Author Contributions:
Conceptualization: Matthew Head
Formal analysis: Matthew Head, Joe Thompson
Investigation: Matthew Head, Joe Thompson
Methodology: Matthew Head
Software: Matthew Head
Supervision: James Hickey
Validation: Matthew Head, James Hickey
Visualization: Matthew Head
Writing – original draft: Matthew Head
Writing – review & editing: Matthew Head, James Hickey, Joachim Gottsmann, Nicolas Fournier

Rheological Controls on Magma Reservoir Failure in a Thermo-Viscoelastic Crust

Matthew Head[1,2] , **James Hickey[1]** , **Joe Thompson[1]**, **Joachim Gottsmann[3]** , **and Nicolas Fournier[4]**

[1]Camborne School of Mines, University of Exeter, Cornwall, UK, [2]Now at Department of Geology, University of Illinois at Urbana-Champaign, Urbana, IL, USA, [3]School of Earth Sciences, University of Bristol, Bristol, UK, [4]GNS Science, Wairakei Research Centre, Taupō, New Zealand

Abstract As volcanoes undergo unrest, understanding the conditions and timescales required for magma reservoir failure, and the links to geodetic observations, are critical when evaluating the potential for magma migration to the surface and eruption. Inferring the dynamics of a pressurized magmatic system from episodes of surface deformation is heavily reliant on the assumed crustal rheology, typically represented by an elastic medium. Here, we use Finite Element models to identify the rheological response to reservoir pressurization within a temperature-dependent Standard Linear Solid viscoelastic ("thermo-viscoelastic") domain. We assess the mechanical stability of a deforming reservoir by evaluating the overpressures required to initiate brittle failure along the reservoir wall, and the sensitivity to key parameters. Reservoir inflation facilitates compression of the ductile wall rock, due to the non-uniform crustal viscosity, impacting the temporal evolution of the induced tensile stress. Thermo-viscoelasticity enables a deforming reservoir to sustain greater overpressures prior to failure, compared to elastic analyses. High-temperature (e.g., mafic) reservoirs fail at lower overpressures compared to low-temperature (e.g., felsic) reservoirs, producing smaller coincident displacements at the ground surface. The impact of thermo-viscoelasticity on reservoir failure is significant across a wide range of overpressure loading rates. By resisting mechanical failure on the reservoir wall, thermo-viscoelasticity impacts dyke nucleation and formation of shear fractures. Numerical models may need to incorporate additional processes that act to promote failure, such as regional stresses (e.g., topographic and tectonic), external triggers (e.g., earthquake stress drops), or pre-existing weaknesses along the reservoir wall.

Plain Language Summary Understanding the conditions required for magma reservoir failure, which can result in the transport of magma to the ground surface, and its links to ground deformation is a persistent challenge when assessing the eruption potential of a volcano. Numerical models are commonly used to account for different complexities observed in nature, which can significantly affect the ambient subsurface stress field or the threshold for reservoir failure. Most numerical models do not consider the impact of crustal behavior; whilst the results can be instructive, an accurate model is of paramount importance when modeling reservoir failure. Here we investigate the conditions for failure within a thermo-viscoelastic crust, accounting for the increased temperatures and ductility surrounding the reservoir. Our results highlight that an inflating reservoir results in the compression of the surrounding crustal rock due to the non-uniform viscosity, which is not observed in simpler elastic models. This hinders the development of the tensile stress, and may require overpressures greater than usually considered to initiate reservoir failure. As the behavior of the crust is controlled by its temperature, and can strongly affect the conditions for reservoir failure, we suggest that thermo-viscoelasticity should be incorporated in deformation models and failure analyses.

1. Introduction

Numerical models are widely used to explore and identify the links between the dynamic evolution of magmatic systems and geodetic and geophysical observations during periods of volcanic unrest (Phillipson et al., 2013), allowing potential eruption precursors to be recognised (Biggs & Pritchard, 2017; Sparks et al., 2012; Tilling, 2008). However, continued periods of ground deformation, or other geophysical phenomena, do not always lead to an eruption (e.g., Biggs et al., 2014; Le Mével et al., 2021; Lundgren et al., 2020; Parks et al., 2015; Wicks et al., 2006). An accurate knowledge of the relationship between geodetic observations and the mechanical stability of a deforming magma reservoir is therefore paramount when assessing the eruptive potential of volcanoes actively undergoing unrest (Acocella et al., 2015; Sparks & Cashman, 2017).

The stress field induced by a deforming reservoir under a given overpressure, and hence its conditions for failure, can be impacted by many factors, including mechanical layering (e.g., Long & Grosfils, 2009), gravitational and edifice loading (e.g., Albino et al., 2018; Grosfils, 2007), surface load variations (e.g., Albino et al., 2010; Satow et al., 2021), and local pore pressure gradients (e.g., Albino et al., 2018; Rozhko et al., 2007), among others. Recent studies incorporate statistical routines to assimilate multiple geodetic observations (e.g., Bato et al., 2017; Zhan & Gregg, 2017) in order to provide constraints on previous eruptive activity (Albright et al., 2019), or to outline potential forecast scenarios (Zhan et al., 2019, 2021), highlighting the capacity for (pseudo-)real-time modeling of the stress fields induced by deforming magmatic systems. To date, the majority of these analyses, along with studies of specific volcanoes (e.g., Browning et al., 2015), assume elastic behavior. The effects of an inelastic crustal rheology on induced stresses and reservoir failure are comparatively less-explored (Cabaniss et al., 2020; Currenti & Williams, 2014; Gerbault et al., 2012, 2018; Gottsmann & Odbert, 2014; Gregg et al., 2012, 2018; Jellinek & DePaolo, 2003; Karlstrom et al., 2010; Ruz-Ginouves et al., 2021). Crustal rheology is a significant component of geodetic models; numerous studies (e.g., Currenti et al., 2010; Got et al., 2013; Hickey et al., 2016; Holohan et al., 2017; Masterlark et al., 2010; Newman et al., 2006) detail the impact on the inferred deformation source characteristics and/or overpressure loading history when incorporating inelastic behavior, compared to a purely elastic model.

Shallow or long-lived magmatic systems can significantly perturb the thermal profile of the local crustal column (e.g., Annen, 2011; Gelman et al., 2013; Karakas et al., 2017), inducing thermomechanical heterogeneity within the surrounding crust; consequently invalidating the elastic approximation. Elevated temperatures facilitate inelastic host rock behavior, comprising viscous effects due to increased ductility, characterizing the rheology of the middle and upper crust (e.g., de Silva & Gregg, 2014). Despite the expectation of inelastic host rock behavior in the region surrounding a magmatic system, field observations show that failure occurs predominantly via brittle, rather than ductile, processes at or near reservoir contacts, as evidenced by the presence of fractures (Gudmundsson, 2020). Analytical models using a viscoelastic shell show that the viscous dissipation of stresses hinder the nucleation and growth of magma-filled fractures (Jellinek & DePaolo, 2003; Rubin, 1993), where the interplay between the timescales of magma injection, internal dynamics, and viscosity of the host-rock determines whether the reservoir ruptures (Degruyter & Huber, 2014; Townsend et al., 2019). This is supported by numerical analyses within an isoviscous domain (Zhan & Gregg, 2019), provided the failure timescales are longer than the viscous timescale of the host rock (i.e., protracted pressurization). A thermo-viscoelastic crustal rheology is increasingly incorporated into geodetic deformation models to account for heterogeneous temperatures and ductility (e.g., Del Negro et al., 2009) that cannot be catered for through analytical approaches (Degruyter & Huber, 2014; Jellinek & DePaolo, 2003; Townsend et al., 2019). Specifically, the non-uniform crustal viscosity is associated with a spectrum of viscous timescales (Head et al., 2021), ranging from near-instantaneous close to the reservoir to many thousands of years toward the ground surface, which has been shown to influence and partition the resulting deformation field (e.g., Gottsmann et al., 2017; Gottsmann & Odbert, 2014; Gregg et al., 2018; Hickey et al., 2016; Le Mével et al., 2016; Morales Rivera et al., 2019). In particular, Head et al. (2021) demonstrate how the rate and amplitude of ground deformation can vary when using a thermo-viscoelastic crustal rheology, depending on the imposed thermal constraints and the chosen linear viscoelastic model. However, there are limited studies that consider the role of thermo-viscoelasticity in terms of modeling reservoir failure, and the impact on induced stresses (e.g., Cabaniss et al., 2020; Gottsmann & Odbert, 2014; Gregg et al., 2012, 2018). This highlights a fundamental gap in the understanding of how a thermo-viscoelastic crustal rheology, based on common implementation after Del Negro et al. (2009), affects the overpressures that can be sustained by a deforming reservoir; whether the influence is either invariant or systematic, and sensitive to key parameters, and whether there are situations where the effects can be considered negligible.

In this study, we: (a) identify rheological phenomena associated with the pressurization of a magmatic reservoir within a thermo-viscoelastic crust; (b) investigate the overpressures required to initiate brittle failure along the reservoir wall; and (c) report the coincident displacements produced at the ground surface by the deforming reservoir. We demonstrate how the critical overpressure can vary with key modeling parameters, including the assumed reservoir temperature, background geothermal gradient, and overpressure loading rate, and highlight the implications for alternative modeling configurations. This study focuses primarily on tensile failure, a requisite for the nucleation and propagation of a magma-filled crack (e.g., Gudmundsson, 2006; Rubin, 1995) that could lead to an eruption, but shear failure is also considered.

2. Numerical Modeling

We use COMSOL Multiphysics® (v5.5) to construct and solve 2D-axisymmetric Finite Element models, coupling the structural mechanics and heat transfer modules to explore the effect of thermomechanical heterogeneity when determining the conditions for reservoir failure. In this study, we evaluate the overpressures required to initiate brittle failure on the reservoir wall within a thermo-viscoelastic crust, as well as the coincident displacements produced at the ground surface. A steady-state temperature field, composed of a background geothermal gradient and the thermal perturbation owing to the modeled reservoir, is used to determine the viscosity distribution within the crust. This study specifically isolates the temporal stress response due to the non-uniform crustal viscosity, and so does not include thermo-elastic effects, such as thermal expansion of the surrounding rock (e.g., Browning et al., 2021) or temperature-dependence of the elastic parameters (e.g., Bakker et al., 2016; Gregg et al., 2012).

2.1. Model Configuration

We build upon the models of Head et al. (2021), adapted from the benchmarked approach of Hickey and Gottsmann (2014), which are displayed schematically in Figures 1a and 1b. The model domain has r- and z-dimensions of 30 km, which features: (a) a free surface on the $z = 0$ plane; (b) an infinite element domain on the lateral edge; and (c) roller boundary conditions on the lateral and basal edges. By definition, the free surface does not support shear stresses and the roller boundaries only allow parallel displacements. The infinite element domain virtually extends the radial dimension of the model, allowing induced stresses and displacements to vanish prior to the roller boundary.

The elastic mechanical properties of the model domain are homogeneous, with a Young's modulus of 30 GPa. The deformation source is represented by a finite spheroidal cavity, with a radius of 1500 m and centered at a depth of 5 km. A uniform excess pressure (i.e., overpressure; ΔP) is applied to the reservoir walls, acting normal to the boundary. The overpressure increases linearly with time, which may represent the continued injection of magma, exsolution of volatiles, or combination thereof. We neglect any second-order dynamical pressure-volume relationships, such as changes in overpressure induced by a change in volume (e.g., Gregg et al., 2013). The numerical models are computed until the failure criteria are met, where the temporal resolution is dependent on the overpressure loading rate, with finer resolutions corresponding to higher rates. For an overpressure loading rate of 1 MPa yr^{-1} the maximum timestep is 1 day, which is robust over the failure timescales involved (i.e., from the onset of overpressure loading to reservoir failure).

2.2. Viscoelastic Rheology

In this study, we use the Standard Linear Solid viscoelastic configuration, which is increasingly incorporated in thermomechanical geodetic models to account for inelastic effects (e.g., Cabaniss et al., 2020; Del Negro et al., 2009; Gottsmann & Odbert, 2014; Gregg et al., 2018; Hickey et al., 2016; Le Mével et al., 2016; Morales Rivera et al., 2019). The rheology is represented conceptually by an elastic spring element in parallel with a Maxwell arm, which itself is formed by an elastic spring and viscous dashpot in series (Fung, 1965; Ranalli, 1995, Figure 1a). The dashpot adds a time-dependent component to the behavior of a solid material, allowing for rheological behaviors such as creep and stress relaxation to be incorporated. For the Standard Linear Solid rheology, the relative contributions of the arms are split according to the weighting of fractional shear moduli, μ_0 and μ_1 (Figure 1a), where $\mu_0 + \mu_1 = 1$. As such, rheological endmembers are characterized by pure elasticity ($\mu_0 = 1$ and $\mu_1 = 0$), and Maxwell viscoelasticity ($\mu_0 = 0$ and $\mu_1 = 1$). The deformation response of the Maxwell rheology is characterized by unbounded creep and complete stress relaxation, describing a viscoelastic fluid (e.g., Banks et al., 2011; Marques & Creus, 2012). Within a Standard Linear Solid configuration, the behavior of the Maxwell arm is modulated by the elastic arm; producing limited, rate-decreasing deformation responses. For detailed comparisons of the Maxwell and Standard Linear Solid viscoelastic models in the context of volcanic ground deformation, see Head et al. (2019) and Head et al. (2021). The viscous component of deformation is commonly assumed to be incompressible; such that volumetric strains are considered to be purely elastic and viscoelastic deformation is represented in terms of the deviatoric strain components (Segall, 2010). This allows the bulk modulus, K, to behave elastically whilst the shear modulus, G, behaves in a viscoelastic manner (Del Negro et al., 2009; Folch et al., 2000). The bulk and shear moduli are determined from the Young's modulus, using standard formulation (Ranalli, 1995; Segall, 2010).
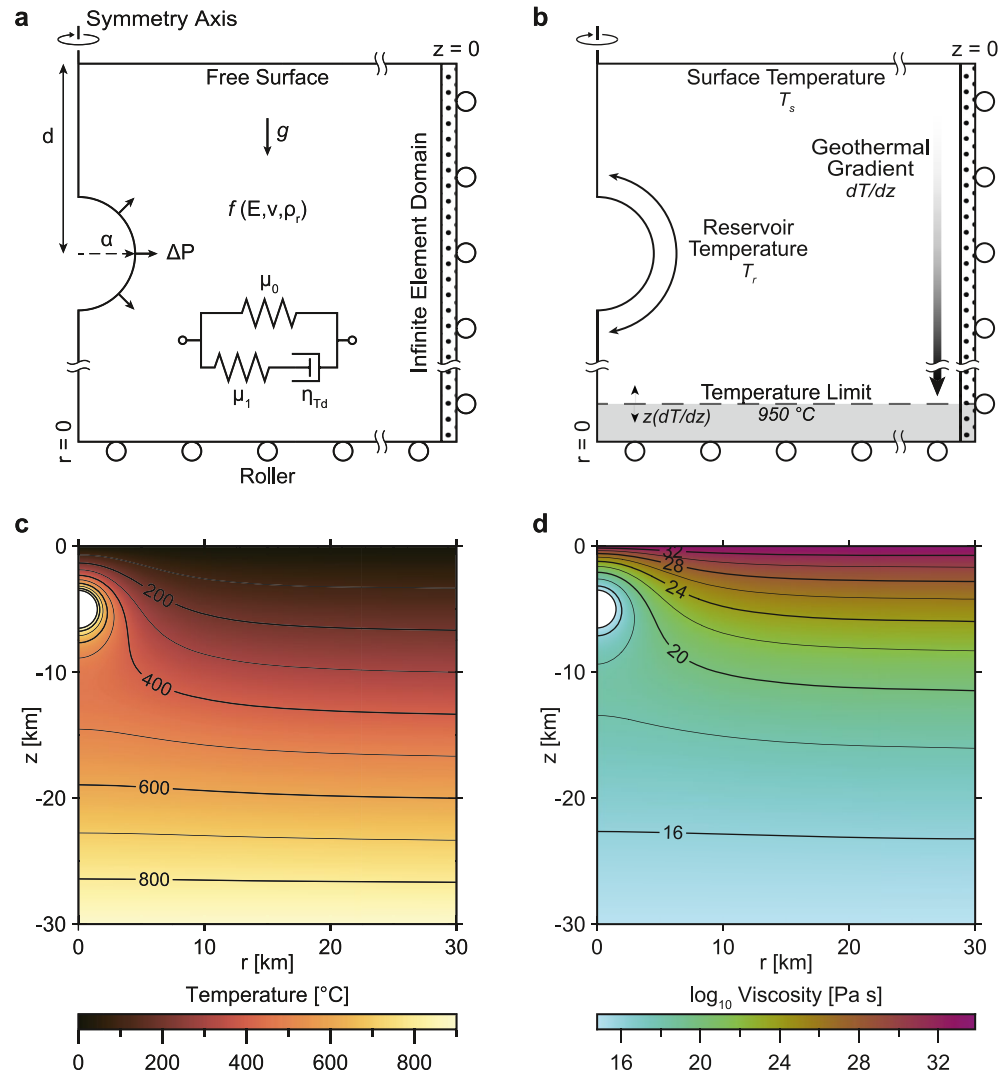
Figure 1. Diagrams of the model configuration. (a) Geometry, boundary conditions, and (b) thermal constraints, where a spherical cavity represents the source of deformation. The Standard Linear Solid viscoelastic rheology (a) is conceptually formed of an elastic spring element and Maxwell arm in parallel, the relative contributions of which are controlled by the fractional shear moduli, μ_0 and μ_1. The imposed geothermal gradients are conservatively limited to a maximum temperature of 950°C (e.g., Schutt et al., 2018), preventing excessive temperatures being produced at depth. (c) An example steady-state temperature distribution and (d) temperature-dependent viscosity (η_{Td}; Equation 1) are shown for a reference model with reservoir temperature, T_r, of 900°C and background geothermal gradient, $\frac{dT}{dz}$, of 30 K km^{-1}.

2.3. Thermal Models

As the timescales associated with deformation and failure are much shorter than the thermal evolution of the magma chamber and the surrounding host rock, we assume that the system has reached thermal equilibrium and compute the temperature distribution of the model domain using the steady-state heat conduction equation (e.g., Del Negro et al., 2009; Gregg et al., 2012). The thermal conductivity, k, and specific heat capacity, C_p, of the crustal column are assumed to be spatially uniform and constant through time; any uncertainties in these values are negligible when determining the steady-state thermal distribution (Hickey et al., 2015; Morales Rivera et al., 2019). The temperature distribution is constrained by fixing the surface temperature, T_s, and background geothermal gradient, $\frac{dT}{dz}$, which is then perturbed locally by the reservoir temperature, T_r. By prescribing a constant temperature to the source boundary, the reservoir walls are considered to be acting as a heat source (Del Negro et al., 2009). A series of thermo-viscoelastic "base" models are used throughout the study, considering a range of reservoir temperatures (Table 1) with a background geothermal gradient of 30 K km^{-1}.

Table 1
List of Model Parameters

Variable	Definition	Dimensions	Value
Source Parameters			
α	Source radius	m	1500
d	Depth	m	5000
$\frac{d\Delta P}{dt}$	Overpressure loading rate	MPa yr^{-1}	1
Model-Space Parameters			
E	Young's modulus	GPa	30
η_{Td}	Temperature-dependent shear viscosity	Pa s	Equation 1
μ_0, μ_1	Fractional shear weightings	-	0.5
ν	Poisson's ratio	-	0.25
ρ_r	Host rock density	kg m^{-3}	2600
T_0	Tensile strength	MPa	10
τ_0	Shear strength	MPa	20
ϕ	Angle of internal friction	°	30
Thermal Parameters			
A_D	Dorn parameter	Pa s	1×10^9
C_p	Specific heat capacity	J kg^{-1} K^{-1}	1200
$\frac{dT}{dz}$	Geothermal gradient	K km^{-1}	30
E_A	Activation energy	J mol^{-1}	1.3×10^5
k	Thermal conductivity	W m^{-1} K^{-1}	3
R	Universal gas constant	J mol^{-1} K^{-1}	8.314
T_r	Reservoir temperature	°C	700, 800, 900, 1000, 1100, 1200
T_s	Surface temperature	°C	0

We use the Arrhenius formulation to calculate the temperature-dependent viscosity structure from the steady-state temperature distribution:

$$\eta_{Td} = A_D \exp \left(\frac{E_A}{RT} \right) \tag{1}$$

where A_D is the Dorn parameter, 1×10^9 Pa s (Del Negro et al., 2009; Gregg et al., 2012; Hickey et al., 2016), E_A is the activation energy, 1.3×10^5 J mol^{-1} (Meissner & Tanner, 1992; Ranalli, 1995), R is the universal gas constant, and T is the absolute temperature. Through this relation, the elevated thermal field induced by the modeled reservoir decreases the viscosity of the surrounding crust (Figure 1d). The crustal column is assumed to be predominantly silicic, producing greater crustal viscosities than expected for a more mafic system (e.g., Morales Rivera et al., 2019). Following the approach of Head et al. (2021), the geothermal gradients are applied to a maximum temperature of 950°C (Figure 1b), a conservative estimate for the deep crust in volcanic regions (e.g., Hickey et al., 2016; Schutt et al., 2018). This ensures that excessively low viscosities are not produced at depth, which may otherwise affect the deformation field. This limit specifically affects models with geothermal gradients greater than 30 K km^{-1}, producing an isothermal and isoviscous region, of $10^{14.4}$ Pa s, at the base of the model. Otherwise, geothermal gradients of 40 and 50 K km^{-1} could produce viscosities as low as $10^{12.2}$ and $10^{11.2}$ Pa s, respectively.

2.4. Failure Criteria

The requirements for the failure of a magma reservoir are determined by calculating the stresses along the reservoir wall. Throughout this study, we adopt the convention that compressive stresses are positive and tensile

stresses are negative. First, gravity is loaded as a body force by applying a lithostatic pressure, P_L, to the model domain:

$$P_L = \rho_r g z \tag{2}$$

where ρ_r is the density of the surrounding host rock, g is gravitational acceleration, and z is the depth below the ground surface (and is therefore negative). The lithostatic load is balanced along the reservoir wall by an initial hydrostatic stress, $-P_L$, returning the system to an equilibrium state such that no net displacements arise from gravitational loading. A uniform overpressure, ΔP, is then applied to the reservoir walls to induce deformation of the surrounding host rock. The total pressure, P_{tot}, on the wall of the modeled reservoir is hence equal to:

$$P_{tot} = -P_L + \Delta P \tag{3}$$

In this study, we apply an overpressure load that increases linearly with time, and so the total pressure, P_{tot}, becomes:

$$P_{tot}(t) = -P_L + \frac{d\Delta P}{dt}(t) \tag{4}$$

where an overpressure loading rate, $\frac{d\Delta P}{dt}$, of 1 MPa yr^{-1} is used for the main portion of this study. Alternative overpressure loading rates, and their effects on reservoir failure, are also explored.

Tensile (or Mode-I) failure, via extension fractures (Gudmundsson, 2006; Jaeger et al., 2007), occurs when the following criterion is satisfied (Albino et al., 2018):

$$-\sigma_3 \geq T_0 + P_L - P_P \tag{5}$$

where σ_3 is the minimum principal (or tensile) stress, P_L is the lithostatic pressure, P_P is the pore fluid pressure, and T_0 is the tensile strength of the surrounding host rock. We also evaluate failure via shear fractures, using the Mohr-Coulomb failure criterion (Jaeger et al., 2007):

$$\tau \geq (\sigma_n + P_L - P_P)\sin\phi + \tau_0\cos\phi \tag{6}$$

where τ is the shear stress, σ_n is the normal stress, τ_0 is the shear strength (or cohesion) and ϕ is the angle of internal friction (assumed to be 30° for silicic crustal rocks; Barton & Choubey, 1977). By isolating the shear strength and expressing in terms of the principal stresses (Jaeger et al., 2007), Equation 6 becomes:

$$\frac{\sigma_1 - \sigma_3}{2\cos\phi} - \left(\frac{\sigma_1 + \sigma_3}{2} + P_L - P_P\right)\tan\phi > \tau_0 \tag{7}$$

Throughout the study we consider the pore fluid pressure to be lithostatic (i.e., $P_P = P_L$), balancing the gravitational load. This results in the failure overpressure being of similar magnitude to the strength (shear or tensile, depending on the mode of failure) of the surrounding rock (e.g., Albino et al., 2018; Gerbault et al., 2012, 2018; Gudmundsson, 2012). The tensile strength of rock is usually assumed to be approximately half that of the shear strength (Gudmundsson, 2011), or one-tenth of its ultimate compressive strength (Jaeger et al., 2007). Tensile strengths measured in situ are expected to vary between 0.5 and 9 MPa (Gudmundsson, 2012), but may be as high as 31 MPa when calculated from laboratory measurements of tensile fracture toughness (Smith et al., 2009; Zhang, 2002). We assume a tensile strength of 10 MPa in our models, with a corresponding shear strength of 20 MPa, which may place an upper bound on the overpressures required for reservoir failure.

3. Thermo-Viscoelastic Response

Viscoelastic rheological models are associated with intrinsic characteristic timescales that govern the rate of viscous processes, such as the creep response and the relaxation of stresses (e.g., Fung, 1969; Head et al., 2021). For the Standard Linear Solid model, the timescales are proportional to the ratio of viscosity, η, to shear modulus, G (e.g., Christensen, 1982):

$$\tau_V = \frac{\eta}{\mu_0\mu_1 G} \tag{8}$$

Table 2
Characteristic Viscous Timescales (to 3 s.f.) for a Range of Temperatures

Temperature, T (°C)	Viscosity, η_{Td} (Pa s)	Viscous timescale, τ_V (d)
400	1.22×10^{19}	4720
500	6.07×10^{17}	2340
600	5.99×10^{16}	231
700	9.51×10^{15}	36.7
800	2.13×10^{15}	8.21
900	6.14×10^{14}	2.37
1000	2.16×10^{14}	0.832
1100	8.82×10^{13}	0.340
1200	4.07×10^{13}	0.157

Note. For the imposed reservoir temperatures (700–1200°C), these are the minimum timescales of the deformation processes.

In an isoviscous domain, viscous stress-strain relationships are controlled by a single timescale (e.g., Head et al., 2019; Zhan & Gregg, 2019). However, the timescales in a thermo-viscoelastic crust are highly heterogeneous due to the non-uniform crustal viscosity (Head et al., 2021). High temperatures near the reservoir wall are associated with short viscous timescales, due to the low viscosity of the material (Figure 1d). As temperatures decrease with distance away from the reservoir, the associated timescales increase. Viscous timescales for a range of temperatures are given in Table 2. Temperatures below 350°C have timescales over 1000 years, which can be considered to behave elastically. Reservoir temperatures ranging from 700 to 1200°C, representing felsic to mafic magma compositions, are used in conjunction with a background geothermal gradient of 30 K km^{-1} to comprise a suite of thermo-viscoelastic "base" models for comparison throughout the study.

The capacity for a viscoelastic material to behave in a viscous manner can be described by the non-dimensional Deborah number, De (e.g., Degruyter & Huber, 2014; Jellinek & DePaolo, 2003; Karlstrom et al., 2010):

$$De = \frac{\tau_V}{t_o} \quad (9)$$

where τ_V is the viscous timescale (Equation 8), and t_o is the period of observation. Here, the period of observation, t_o, simply relates to the duration of a pressurization episode (i.e., loading timeframe), however its form may vary depending on the criteria (e.g., a characteristic strain) and/or physics considered (e.g., magma injection; Degruyter & Huber, 2014; Jellinek & DePaolo, 2003; Karlstrom et al., 2017). A viscoelastic material behaves in an elastic manner at large values of De (>>1), whereas small values of De (<<1) indicate viscous behavior. Viscous effects are shown to begin around $De = 10$ (Rucker et al., 2022). The Standard Linear Solid rheology is characterized by a finite viscous response, which is effectively saturated at $De = 0.2$ (>99% of the viscous response occurs within $5 \tau_V$). Figure 2 illustrates how De varies as a function of temperature, using the viscous timescales within Table 2, and the duration of overpressure loading. Importantly, Figure 2 indicates the parameter-space (above the $De = 10$ dotted line) for which the viscous response is non-negligible.

3.1. Case 1: Constant Overpressure

In elastic media, the tensile stress on the reservoir wall is linearly proportional to the applied overpressure (Figure 2a; Jaeger et al., 2007; Tait et al., 1989). For a spherical reservoir within a full-space, the tensile stress is half of the applied overpressure (i.e., $\frac{\Delta P}{\sigma_3} = 2$; Jaeger et al., 2007; Tait et al., 1989). Due to the finite model domain (half-space) and the influence of the free surface (e.g., Grosfils, 2007), the ratio is approximately 1.9 (Figure 2a). However, the ratio can vary further depending on the depth and geometry of the deformation source, as well as the imposed stress fields (e.g., edifice loading; Albino et al., 2018). In response to a constant overpressure, the tensile stress of the thermo-viscoelastic models evolve through time (Figure 3a); the magnitude quickly decays, before recovering toward the elastic value over the long term. Cross-sections of volumetric strain (Figures 3b
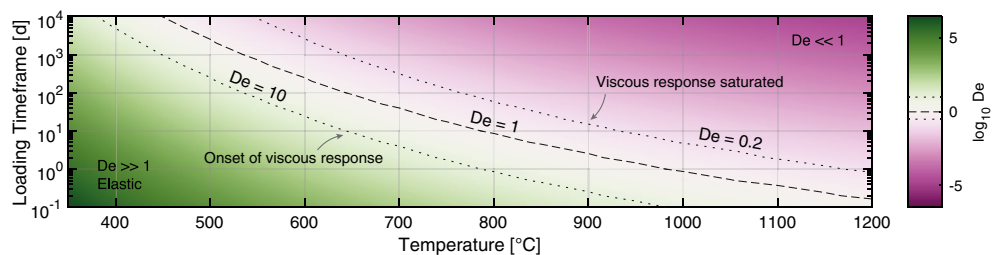

Figure 2. Deborah number (De; Equation 9) as a function of temperature and duration of overpressure loading for the thermo-viscoelastic Standard Linear Solid rheology. The $De = 1$ dashed line marks the equivalence of the viscous timescale, τ_V, and the period of observation, t_o. Viscous behavior begins at around $De = 10$, and the viscous response of the Standard Linear Solid rheology is saturated at $De = 0.2$.
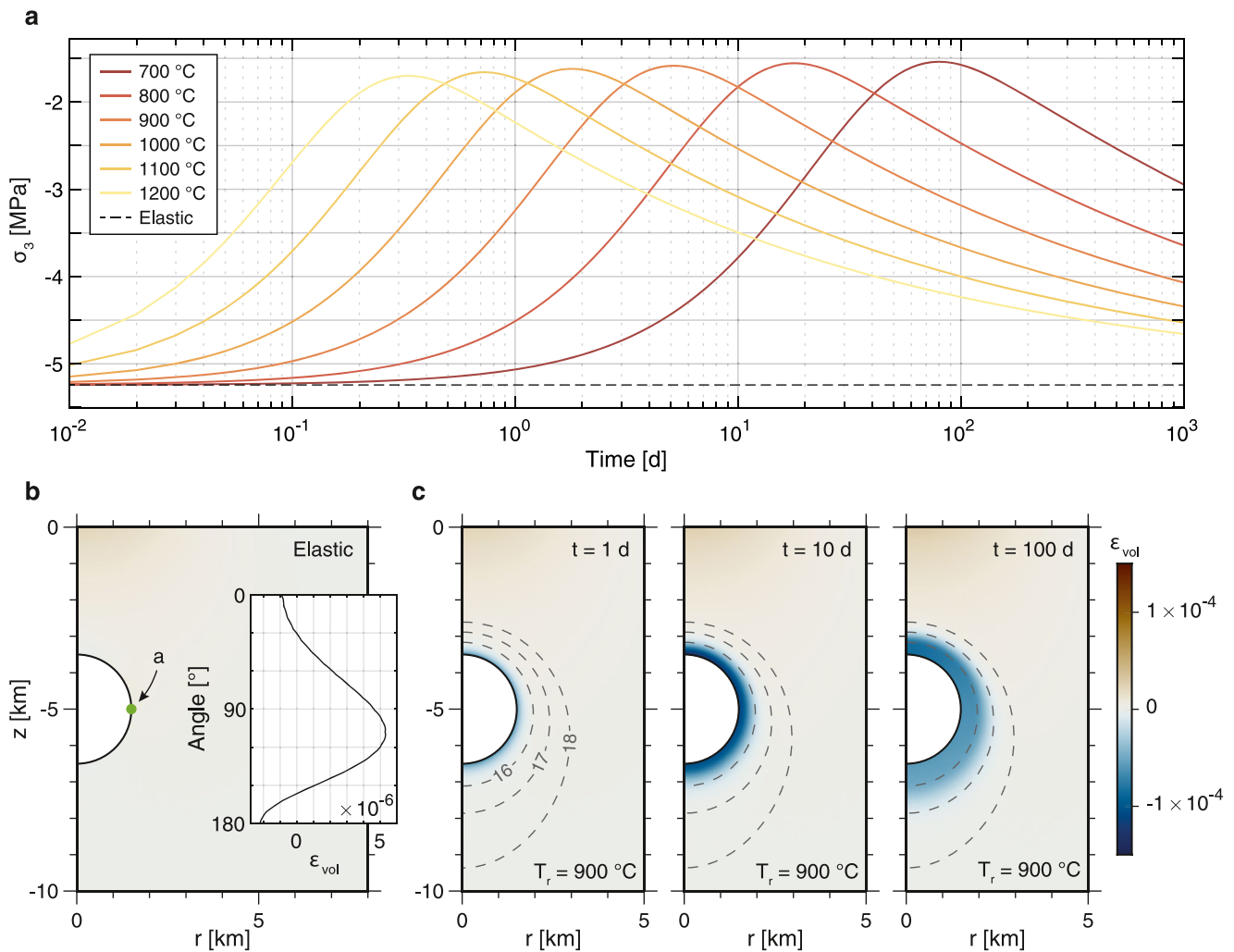
Figure 3. Effect of a constant overpressure load (10 MPa) on tensile stress (σ_3) and volumetric strain (ε_{vol}). (a) For the thermo-viscoelastic models, tensile stress (σ_3) on the reservoir wall (sampled at the lateral edge of the reservoir, shown in (b)) decreases in magnitude over short timeframes and is followed by a long-term recovery toward the elastic model. The rate is controlled by the host rock viscosity, where high temperatures produce low viscosities with short characteristic timescales. (b) Cross-section of volumetric strain (ε_{vol}) for the elastic model, which exhibits minor partitioning of the deformation field along the reservoir boundary; shown as a function of the angle from the reservoir apex in the inset plot. (c) For a thermo-viscoelastic model, cross-sections of volumetric strain demonstrate that the applied overpressure induces a region of compression. The magnitude of the compressive strain varies through time, corresponding to the tensile stress (a), whilst the spatial footprint increases. Viscosity contours ($\log_{10}$ Pa s) are shown by dashed gray lines.

and 3c) illustrate that reservoir inflation compresses the surrounding crust in a way that is not observed in the elastic model (Figure 3b). Despite compression of the host-rock, the reservoir wall itself remains in tension at all times (Figure 3a).

Compression is caused by the range of viscous timescales associated with the heterogeneous viscosity distribution. Over short timeframes (e.g., 10 days), appreciable viscous deformation is limited to low-viscosity (high-temperature) material close to the reservoir wall (i.e., with a low *De* value; Figure 2). As cooler (i.e., more-viscous) rocks away from the reservoir cannot sufficiently deform in a viscous manner (i.e., a greater *De* value; Figure 2); strain accumulates within the hot material around the reservoir, inducing an aureole of compression (Figure 3c). This causes the tensile stress along the reservoir wall to decrease in magnitude over short timeframes (Figure 3a). A significant characteristic of the Standard Linear Solid rheology is a finite strain response to the application of stress; after some time, low-viscosity material reaches the strain limit and cannot deform further (without an increase in the overpressure load). Over longer timeframes (e.g., 100 days), more-viscous (i.e., cooler) material away from the reservoir can deform viscously (as the *De* value is reduced; Figure 2), dissipating the accumulated strain near the reservoir. The region of compression decreases in magnitude and

becomes more diffuse, and the tensile stress recovers toward that of the elastic model (Figures 3a and 3c). The viscous timescales increase exponentially away from the reservoir (up to a maximum timescale of $>10^{16}$ years, corresponding to the ground surface); the tensile stress cannot recover completely and therefore does not reach that of the elastic model. As compression arises due to an inherent lag in viscous timescales, it does not occur in media of uniform viscosity.

3.2. Case 2: Linearly Increasing Overpressure

The response to a variable overpressure load is controlled by the Boltzmann superposition principle, whereby each increment of load produces an independent and additive contribution to the stress state. For a linearly increasing overpressure, the stress and strain responses identified in Figure 3 are continuously superposed through time, proportional to the load increment, as shown in Figure 4. For the elastic model, the magnitude of the tensile stress increases linearly (Figure 4a). The tensile stress of the thermo-viscoelastic models also increases in magnitude with the applied overpressure, but the difference with respect to the elastic model increases with continued pressurisation (Figure 4a). Over short timeframes, the reservoir deforms with high initial strain-rates (Figure 4b), reflecting the short viscous timescales of the high-temperature host rock immediately surrounding the reservoir. Through time, the strain-rate decreases as the deformation is increasingly controlled by the longer timescales of cooler material further from the reservoir. Over a given period, low-temperature reservoirs exhibit reduced rates of deformation relative to high-temperature reservoirs, as is similarly observed with tensile stress (Figure 4a). Figure 4 illustrates the spatiotemporal changes in tensile stress (Figures 4c and 4d) and volumetric strain (Figures 4e and 4f) within the surrounding host rock, sampled at overpressures of 1 and 10 MPa. Continued pressurisation increases the magnitude of both the tensile stress (Figures 4a–4d) and induced compression (Figures 4e and 4f), alongside an expanding spatial footprint and diminishing strain-rate (Figure 4b). Cross-sections of the second invariant of deviatoric strain are shown in Figure S1 in Supporting Information S1. Within an elastic medium, the tensile stress and volumetric strain decay exponentially with increasing distance from the reservoir wall, as shown by the profiles in Figures 4c–4f. However, the thermo-viscoelastic models exhibit a tensile stress "pulse" in response to the onset of overpressure loading and induced compression, decreasing in amplitude as it propagates away from the reservoir through time (Figures 4c and 4d). Close to the reservoir wall, the tensile stress can be of significantly lower magnitude than the elastic model, due to the "shadow" of the propagating impulse after it has passed. The compressive strain decays away from the reservoir with an approximate sigmoid trend (Figures 4e and 4f), with the distal (i.e., right-most) change in gradient approximately coincident with the tensile stress impulse (Figures 4c and 4d). Changes in tensile stress and volumetric strain at the roof of the reservoir are shown in Figure S2 in Supporting Information S1.

The length-scale and magnitude of the compressive aureole (e.g., Figures 4e and 4f) is highly dependent on the viscous timescales (i.e., temperature field) of the crust, which are highly heterogeneous, the overpressure loading history (i.e., duration and magnitude), as well as the dimensions of the deformation source. Given that any application of, or increase in, overpressure induces proportionate compression within the surrounding host rock, there are significant implications for processes that involve the tensile stress, such as brittle failure along the reservoir wall.

4. Impact on Reservoir Failure

The analysis presented in the prior section illustrates the influence of the thermo-viscoelastic rheology on the minimum principal (tensile) stress. Here we provide results for the overpressures required to initiate brittle failure on the reservoir wall (termed "critical overpressure") and the coincident vertical displacement produced at the ground surface, with an overpressure loading rate of 1 MPa yr^{-1} unless otherwise stated. This section primarily focuses on tensile failure, but shear failure is briefly considered. Results are normalized to the corresponding elastic model throughout. We consider a series of "base" thermo-viscoelastic models, indicated by a dashed trendline within each figure, as a basis for comparison when varying key model parameters. These base models cover the range of reservoir temperatures (700–1200°C), with the following default parameters (Table 1): Geothermal gradient of 30 K km^{-1}, overpressure rate of 1 MPa yr^{-1}, fractional shear moduli of 0.5, and a spherical geometry.
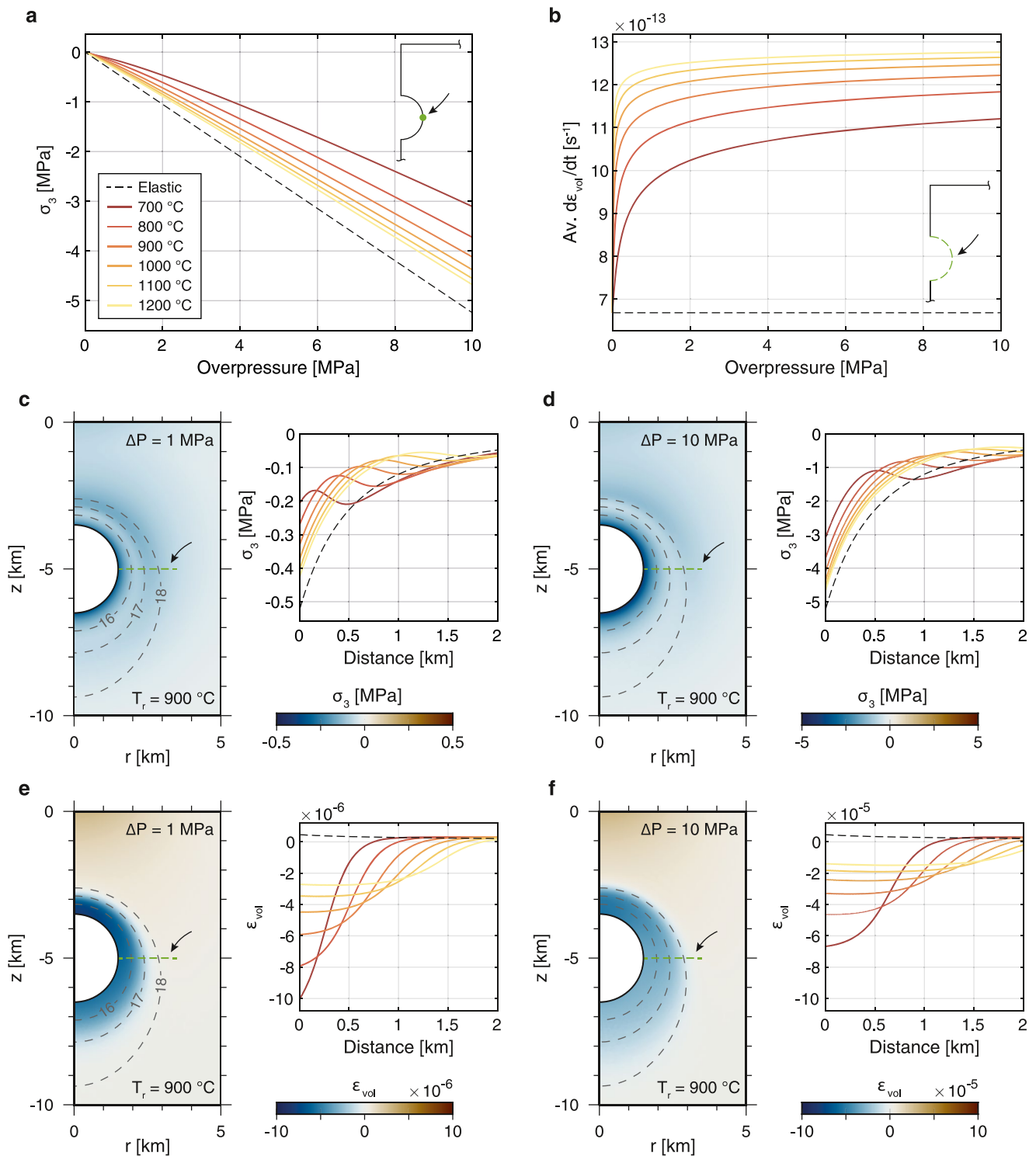
Figure 4. Temporal and spatial evolution of tensile stress (σ_3), volumetric strain (ε_{vol}) and strain-rate ($\frac{d\varepsilon_{vol}}{dt}$), with a linearly increasing overpressure load of 1 MPa yr^{-1}. (a) The tensile stress (σ_3) of the thermo-viscoelastic models (sampled at the lateral edge of the reservoir) diverges from the elastic model with time, due to the long-term temporal evolution (Figure 3a). (b) Volumetric strain-rates (averaged along the reservoir wall) in a thermo-viscoelastic crust increase logarithmically with overpressure, with high initial deformation rates. Within an elastic medium, the reservoir deforms at a constant rate. (c) Cross-section and spatial profile of tensile stress (σ_3) at an overpressure of 1 MPa. (d) As (c), but at an overpressure of 10 MPa. (e) Cross-section and spatial profile of volumetric strain (ε_{vol}) at an overpressure of 1 MPa. (f) As (e), but at an overpressure of 10 MPa. The profiles are normal to the lateral edge of the reservoir, as shown in the cross-sections (green dashed lines). Viscosity contours ($\log_{10}$ Pa s) are shown by dashed gray lines. Note the different color scales.
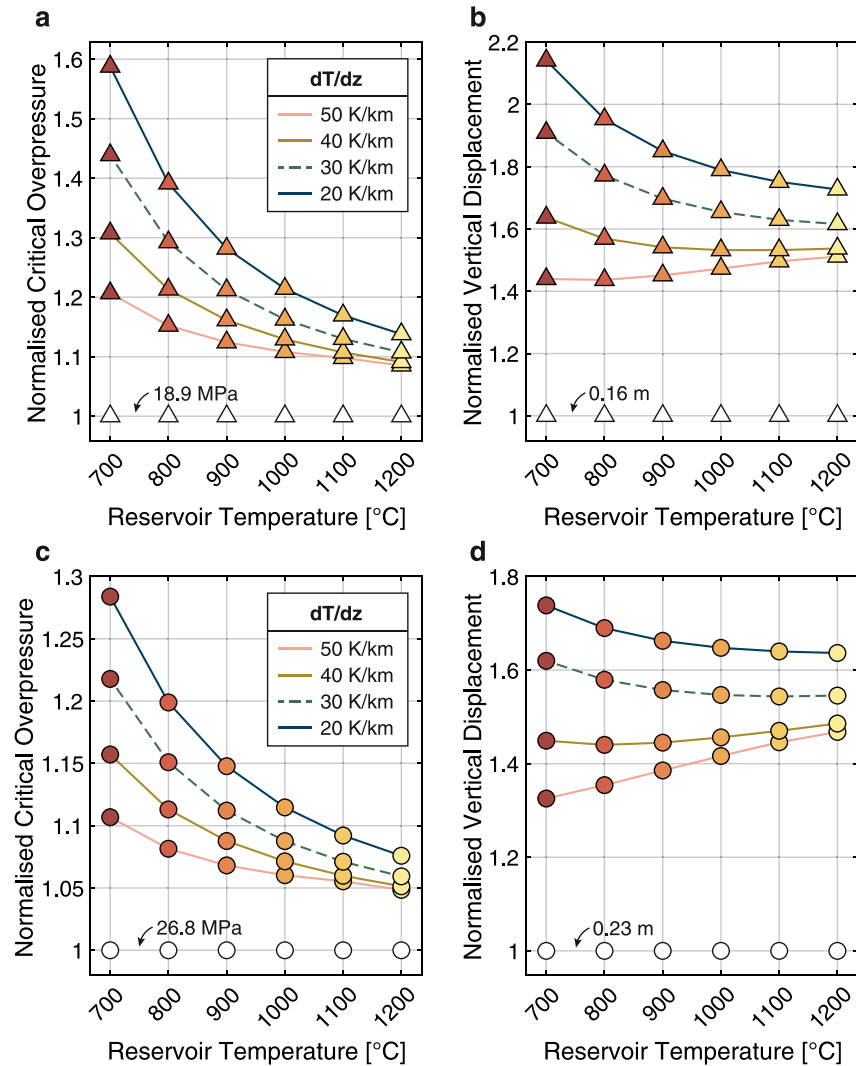
Figure 5. Impact of varying thermal constraints on brittle failure and ground deformation. Results are normalized by the elastic model, indicated on the plots, and the "base" model suite is indicated by a dashed trendline. (a) Overpressure required to initiate tensile failure on the reservoir wall. (b) Coincident vertical displacement at the ground surface ($r = z = 0$). (c) Overpressure required to initiate shear failure on the reservoir wall. (d) Coincident vertical displacement at the ground surface ($r = z = 0$). Hollow markers depict elastic results, unaffected by the thermal conditions, whilst thermo-viscoelastic results are shown by solid markers, colored by reservoir temperature. Thermo-viscoelasticity enables the reservoir to sustain greater overpressures prior to failure and produce elevated deformation relative to the elastic model. Critical overpressures and displacements are maximized for low reservoir temperatures and/or geothermal gradients.

4.1. Imposed Thermal Constraints

In this section, we demonstrate the effect of variable thermal constraints on reservoir failure within a thermo-viscoelastic crust. The elastic model reaches tensile failure at a critical overpressure of ∼18.9 MPa (Figure 5a), producing 0.16 m of coincident vertical displacement (Figure 5b) at the ground surface directly above the modeled reservoir (i.e., $r = z = 0$), whilst shear failure occurs at an overpressure of ∼26.8 MPa (Figure 5c) with 0.23 m of coincident vertical displacement (Figure 5d). These overpressures may be considered to be relatively high, due to the chosen failure parameters (i.e., potential upper limits) and the spherical reservoir geometry, which does not concentrate the applied stress (e.g., Zhan & Gregg, 2019).

For the suite of thermo-viscoelastic models, there are clear trends across both the critical overpressures and the coincident vertical displacements (Figure 5). Overall, the thermo-viscoelastic crustal rheology allows the
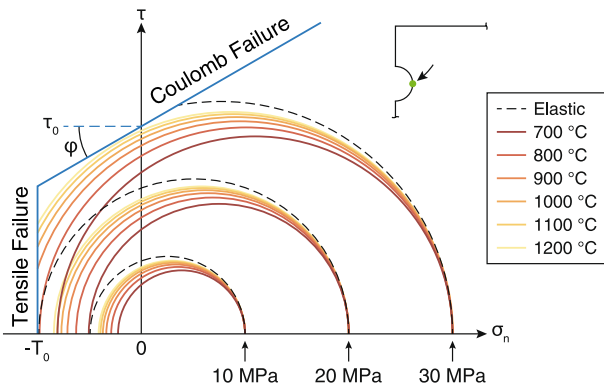
Figure 6. Mohr circles illustrate the effect of thermo-viscoelasticity on reservoir failure. Increased overpressures are required to cross the failure envelope, relative to the elastic model, due to the reduced tensile stress. Critical overpressures are maximized for low-temperature reservoirs. Stresses are sampled at the lateral edge of reservoir, as shown by the inset diagram, at 10 MPa intervals. The models shown have a geothermal gradient of 30 K km^{-1}.

reservoir to sustain greater overpressures relative to the elastic model, inhibiting mechanical failure (e.g., Cabaniss et al., 2020; Gregg et al., 2012), in-line with the earlier analysis of the tensile stress (Figure 4a). This general result is also in agreement with those of alternative viscoelastic implementations (e.g., Jellinek & DePaolo, 2003; Karlstrom et al., 2010; Rubin, 1993). Figure 5 shows that critical overpressure is inversely proportional to the reservoir temperature and geothermal gradient; maximized for cool thermal conditions (e.g., 700°C and 20 K km^{-1}) and minimized for hot thermal conditions (e.g., 1200°C and 50 K km^{-1}). Across the parameters investigated here, the reservoir can sustain overpressures that are up to 60% greater than that of the elastic model before tensile failure occurs (Figure 5a), varying between ∼10% and ∼45% greater when considering a "standard" continental geotherm of 30 K km^{-1}. Similar trends are observed with the overpressure required for shear failure (Figure 5c), up to 30% greater than the overpressures required for failure in an elastic medium. Shear failure is less affected by the thermo-viscoelastic crustal rheology, as the failure criterion is also dependent on the maximum principal stress (σ_1) as a component of both the normal and shear stress (Equation 7), which acts to modulate the tensile stress response (σ_3; Figure 4a).

The vertical displacements exhibit similar patterns to the critical overpressure, inverse proportionality to reservoir temperature and geothermal gradient; except at high geothermal gradients (Figures 5b and 5d). Head et al. (2021) demonstrate that the rate of displacement, and therefore the displacement achieved over a given timeframe, is (a) dependent on the imposed thermal constraints, and (b) becomes near-linear due to the asymptotic (strain-limited) nature of the Standard Linear Solid deformation response (e.g., Fung, 1965; Head et al., 2019). High geothermal gradients affect the partitioning of deformation along the reservoir wall, reducing the displacement attained at the ground surface, whilst high-temperature reservoirs increase the amplitude of surface deformation (Head et al., 2021). As a result, the vertical displacements for low-temperature reservoirs (e.g., 700°C) do not scale directly with the increasing critical overpressures (Figures 5a and 5c), and the relationship between critical overpressure and vertical displacement varies with the geothermal gradient (Figures 5b and 5d). The ground deformation at the time of tensile failure can be between 40% and 120% greater than the displacements produced by an elastic model, or between 30% and 75% greater when shear failure occurs. As with the critical overpressure, the relative deformation at the time of shear failure is lower than for tensile failure. Additionally, Figure 5 highlights that the critical overpressures and ground displacements of low-temperature reservoirs are more sensitive to variations in the assumed geothermal gradient. Fundamentally, Figure 5 demonstrates that the critical overpressure required to initiate tensile or shear failure can vary significantly with the imposed thermal constraints.

The critical overpressure results of Figure 5 can be represented by Mohr circle diagrams (Figure 6), to demonstrate the impact of thermo-viscoelasticity in an alternative manner. The Mohr circles are sampled at the lateral edge of the reservoir wall (as shown by the inset diagram) for applied overpressures of 10, 20, and 30 MPa, with the thermo-viscoelastic models exhibiting decreased tensile stress (σ_3; left-hand side of the Mohr circles) with respect to the elastic model. This result directly impacts the overpressure required to cross the failure envelope and initiate reservoir failure, with critical overpressures maximized for low-temperature reservoirs. Figure 6 shows that the thermo-viscoelastic models with reservoir temperatures of 700°C and 800°C require an overpressure greater than 30 MPa (i.e., the right-most Mohr circles) to surpass the tensile failure criterion at the sample point, whereas the other models have already undergone tensile failure. At this sample point, only the elastic model has reached shear failure. The assumed geothermal gradient controls the ambient viscosity around the reservoir, with a secondary impact on the critical overpressure (Figures 5a and 5c), and would alter the size and position of the Mohr circles.

The thermo-viscoelastic crustal rheology does not just affect the overpressure that can be sustained by a deforming reservoir, but also the location where rupture initiates. Figure 7 displays the 10 MPa tensile stress contour, corresponding to the tensile strength of the host rock, along the reservoir wall as a function of the applied overpressure. As such, failure initiates at the angle corresponding to the minimum overpressure along the contour; the
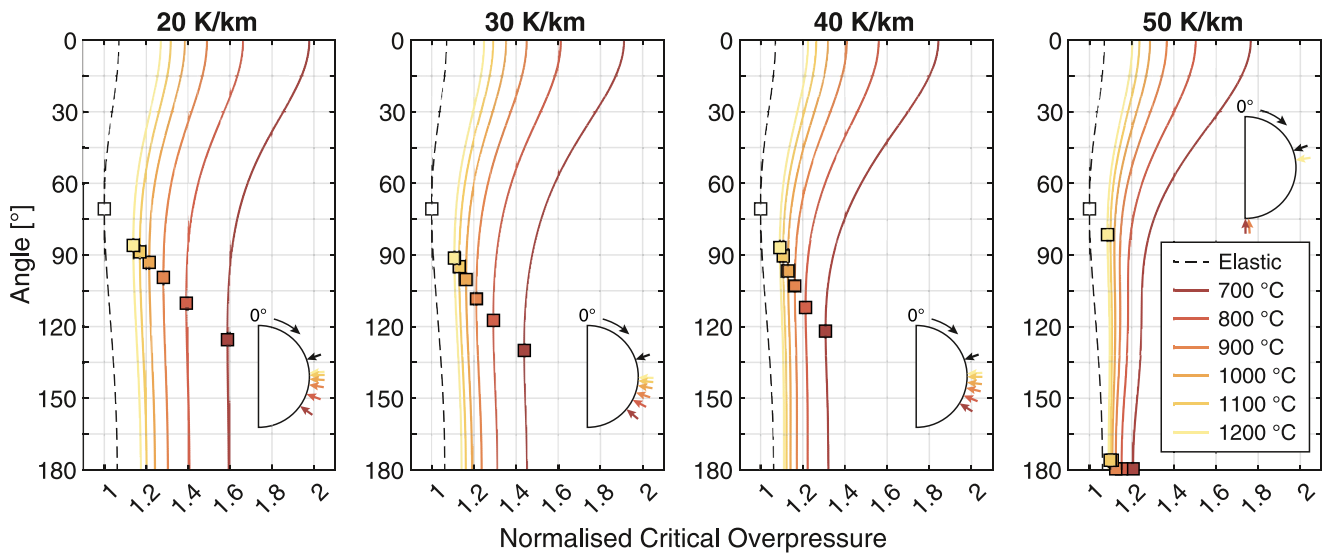
Figure 7. Effect of the thermo-viscoelastic crust, and variation in thermal parameters, on the failure angle along the reservoir wall. Lines are the 10 MPa tensile stress contour (i.e., the tensile strength) as a function of the angle from the reservoir apex and applied overpressure. Failure location is marked by the filled square, which occurs at the angle corresponding to the minimum overpressure along the contour (i.e., the critical overpressure). In the elastic model, failure occurs at an angle 70.7°. Increased failure angles are observed within a thermo-viscoelastic crust, generally occurring within, or close to, the lower hemisphere of the reservoir. The angle is inversely proportional to the reservoir temperature, and varies slightly for geothermal gradients of 20, 30 and 40 K km^{-1}. Deformation partitioning due to high background geothermal gradients (i.e., 50 K km^{-1}; Head et al., 2021) can cause failure to occur at the base of the reservoir.

normalized critical overpressure reported in Figure 5a. Using a similar analysis for shear failure, our models indicate that both tensile and shear failure initiate at the same location (Figure S3 in Supporting Information S1). For the elastic model, failure initiates at an angle of 70.7° from the vertical (measured clockwise from the reservoir roof), consistent with the analytical expression for the location of maximum hoop stress (e.g., McTigue, 1987) and the numerical results of Albino et al. (2018). In a thermo-viscoelastic crust, reservoir temperature is a key control on the failure location along the reservoir wall, occurring either within, or toward, the lower hemisphere of the reservoir. The failure angle increases for low-temperature reservoirs, due to partitioning of the stress field and the associated viscous timescales. Steep viscosity gradients above the reservoir, caused by the thermal constraint of the ground surface (Figures 1c and 1d), also mean that the lower portion of the reservoir is surrounded by crustal material that is more compliant. Minor variations in failure angle (±10°) are observed for geothermal gradients of 20–40 K km^{-1}, with failure of high-temperature reservoirs occurring around the lateral vertex (∼90°). High geothermal gradients cause low ambient viscosities around the reservoir, which preferentially partition deformation toward the base of the reservoir (Head et al., 2021). This can substantially affect the rupture location, as observed for a geothermal gradient of 50 K km^{-1}. When assuming a spherical reservoir geometry, the rupture angle along the reservoir wall may influence the position of eruptive vents at the ground surface, relative to the deformation center (e.g., Ebmeier et al., 2018; Lerner et al., 2020), by altering the trajectory of magma-filled cracks (e.g., Dahm, 2000; Gudmundsson, 2006). Specifically, this could be investigated with further analogue experiments and numerical modeling (Kavanagh et al., 2018).

4.2. Rate of Overpressure Loading

Whilst the prior results utilize an overpressure loading rate of 1 MPa yr^{-1}, overpressures employed in geodetic modeling studies are typically dependent on the goodness-of-fit of the model, in terms of reproducing the observed deformation patterns. This generally involves a trade-off between source size and magnitude of overpressure, unless the size can be independently constrained. Here we consider a wide range of overpressure loading rates, from 0.1 to 100 MPa yr^{-1} to explore the impact on the viscous response (Figure 8). Our results illustrate that critical overpressures increase with the rate of overpressure loading, relating to the tensile stress response following the application of overpressure (Figure 3b). Over short timeframes, the magnitude of the tensile stress is greatly decreased with respect to the elastic model. High overpressure loading rates therefore need to be applied for a longer period for the tensile stress to reach the tensile strength, which results in elevated critical overpressures
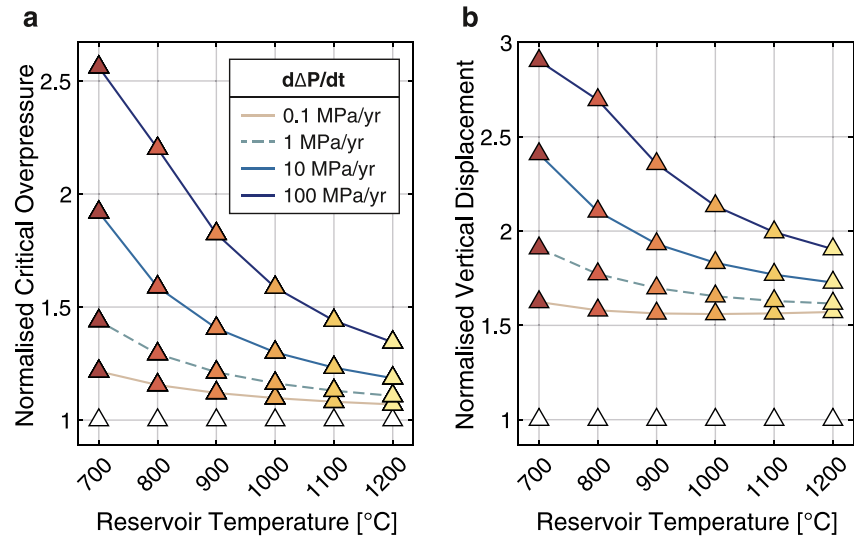
Figure 8. Impact of overpressure loading rate on tensile failure and ground deformation. Results are normalized by the elastic model (18.9 MPa and 0.16 m), and the "base" model suite is indicated by a dashed trendline. (a) Overpressure required to initiate tensile failure on the reservoir wall. (b) Coincident vertical displacement at the ground surface ($r = z = 0$). The plots illustrate that rate of overpressure loading is a key control on the relative stability of the deforming reservoir in a thermo-viscoelastic crust, with critical overpressure and surface displacements increasing with loading rate. Hollow markers depict elastic results, unaffected by the overpressure loading rate, whilst thermo-viscoelastic results are shown by solid markers, colored by reservoir temperature.

(Figure 8a) and increased deformation at the ground surface (Figure 8b). Even over extended failure timescales produced by a low loading rate of 0.1 MPa yr^{-1}, critical overpressures can increase by up to 25% (Figure 8a), and displacements by over 50% (Figure 8b), relative to the elastic model. Ultimately, these results demonstrate that thermo-viscoelasticity affects both critical overpressures and surface displacements across a wide range of over-pressure loading rates, and therefore should not be neglected when assessing the stability of a deforming reservoir and the associated geodetic observations (Figure 8).

4.3. Fractional Shear Moduli and Maxwell Viscoelasticity

A consideration when using the Standard Linear Solid rheology is the weighting of the fractional shear moduli, controlling the proportion of elastic ($\mu_0 = 1$, $\mu_1 = 0$) to Maxwell viscoelastic ($\mu_0 = 0$, $\mu_1 = 1$) behavior. Due to a lack of constraints (observed, experimental, or otherwise) an equal weighting of the fractional shear moduli ($\mu_0 = \mu_1 = 0.5$) is the default choice. Head et al. (2019) detail the effect of varying the fractional shear moduli on the surface displacements that arise in response to a constant overpressure, and an isolated study uses an increased weighting of the elastic arm ($\mu_0 = 0.7$) to improve the goodness-of-fit of model results to observed data (Currenti, 2018). Figure 9a shows that the overpressure required to initiate reservoir failure increases exponentially as the viscoelastic fractional shear modulus tends toward Maxwell viscoelastic (i.e., $\mu_0 = 0$), as also observed with the vertical displacements (Figure 9b). Figure 9c shows the temporal evolution of the tensile stress in response to the application of a constant overpressure (cf. Figure 3a), with a reservoir temperature of 900°C, for different elastic fractional shear moduli. The elastic arm of the Standard Linear Solid model modulates the viscous response of the Maxwell arm, controlling the tensile stress responses observed in Figure 9c. Decreasing the weight of the elastic arm increases the proportion of viscous behavior, increasing the overpressure that can be sustained prior to reservoir failure (Figure 9a). The coincident surface displacements (Figure 9b) are also elevated as a result of (a) the increased failure timescales, and (b) an increased component of viscous deformation, dependent on the fractional shear moduli (e.g., Crawford, 1998; Head et al., 2019). However, a pure Maxwell rheology (i.e., $\mu_0 = 0$) does not undergo failure along the reservoir wall, as inherent fluid behavior prevents the necessary tensile stress from being achieved (e.g., Banks et al., 2011; Marques & Creus, 2012). Further to this, Head et al. (2021) demonstrate that the Maxwell thermo-viscoelastic crust can produce significant subsidence at the ground surface over extended periods of overpressure loading, partitioning the unbounded
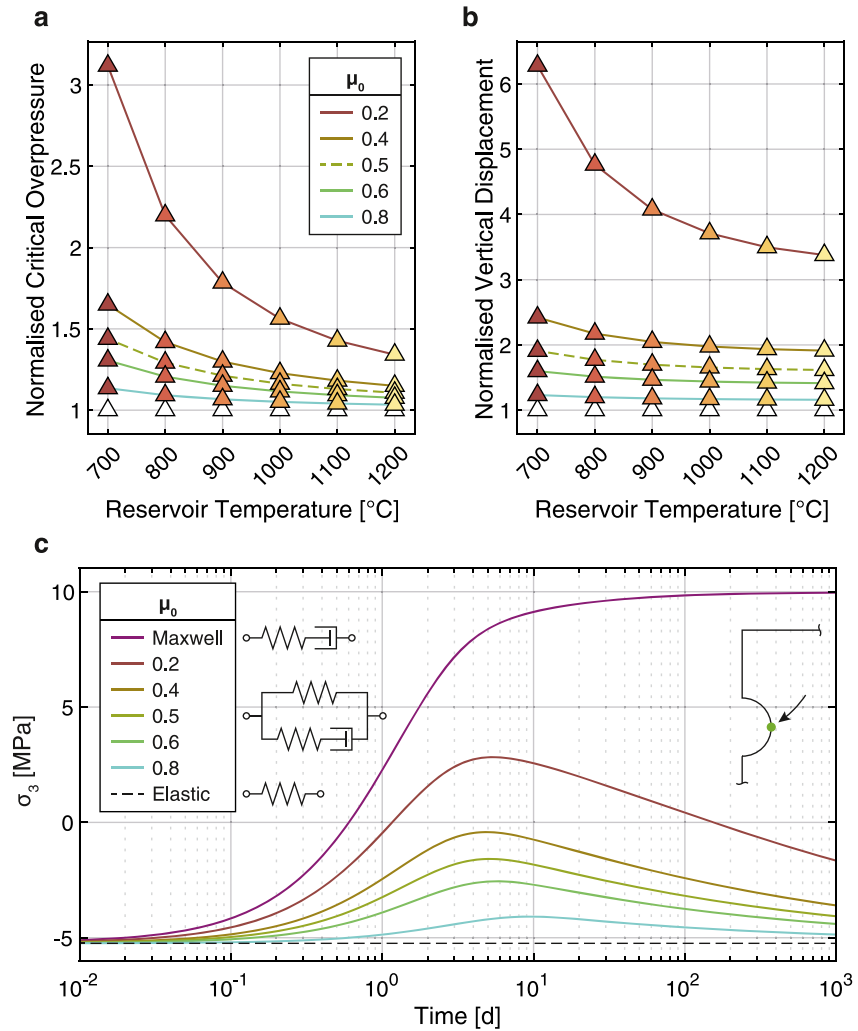
Figure 9. Impact of the fractional shear moduli weighting on tensile failure and ground deformation. Results are normalized by the elastic model (18.9 MPa and 0.16 m), and the "base" model suite is indicated by a dashed trendline. (a) Overpressure required to initiate tensile failure on the reservoir wall. (b) Coincident vertical displacement at the ground surface ($r = z = 0$). Hollow markers depict elastic results, whilst thermo-viscoelastic results are shown by solid markers, colored by reservoir temperature. Critical overpressure and ground deformation increase exponentially as the elastic fractional shear modulus (μ_0) decreases from 1 (elastic; hollow markers) toward 0 (Maxwell viscoelastic). (c) Evolution of the tensile stress (σ_3) due to a constant overpressure load (10 MPa; cf. Figure 3a) for different fractional shear moduli weightings. Data is sampled at the lateral edge of the reservoir (shown by inset) and corresponds to a reservoir temperature of 900°C. The elastic arm (i.e., $\mu_0 > 0$) enables long-term recovery of the tensile stress, whereas the tensile stress dissipates fully over time within a Maxwell thermo-viscoelastic medium ($\mu_0 = 0$, $\mu_1 = 1$), equaling the applied overpressure. Reservoir failure is not achieved in a pure Maxwell rheology.

deformation response in regions of low ambient viscosity (i.e., the base of the reservoir). As such, the use of Maxwell thermo-viscoelasticity should be carefully considered.

An alternative implementation for the Maxwell rheology takes the form of viscoelastic shells embedded within an elastic medium (e.g., Dragoni & Magnanensi, 1989; Newman et al., 2001) where, within a spatially-finite shell, the induced stresses equilibrate and become equal to the applied overpressure with time. However, this configuration only allows for brittle failure to occur at the rheological interface between the viscoelastic shell and surrounding elastic crust. Fundamentally, the application of the Maxwell rheology is dependent on the problem being addressed; a localized region surrounding a magma reservoir may be suitably characterized as a viscoelastic fluid if the crack density and magma-saturation is sufficient (e.g., Dragoni & Magnanensi, 1989;

O'Connell & Budiansky, 1977), whereas Maxwell viscoelasticity is likely an inappropriate choice of rheology for a crustal-scale viscoelastic domain representing solid rock with increased ductility.

4.4. Reservoir Geometry

Deviations away from the idealized spherical geometry act to concentrate imposed stresses, resulting in partitioned deformation and reservoir failure at reduced overpressures (e.g., Currenti & Williams, 2014; Gerbault et al., 2018; Zhan & Gregg, 2019). In this section we consider reservoir geometries with different aspect ratios, ranging from 1/5 (prolate) to 5 (oblate). Each geometry has the same surface area as the spherical reservoir, so that the total force applied is equal. These reservoirs are centered at a depth of 5 km beneath the free surface, as with the spherical reservoir, which increases the roof thickness for oblate geometries whilst decreasing the roof thickness for prolate geometries. Figure 10 presents cross-sections of volumetric strain for oblate and prolate reservoir geometries, with aspect ratios of 3 and 1/3 respectively, illustrating that strain concentration at the reservoir vertices produces regions of relative tension and compression (Figure 10). Due to this inherent partitioning, the viscous strain response (Figures 10c and 10f) can be isolated by removing the elastic strain (Figures 10a and 10d) from that of the thermo-viscoelastic models (Figures 10b and 10e); highlighting that the induced compression, in response to overpressure loading, is independent of the reservoir geometry. It is interesting to note a localized region of tension at the base of the prolate reservoir (Figure 10c).

The normalized critical overpressures and coincident vertical displacements vary with the specific reservoir geometry used (Figure 11). Each reservoir geometry is normalized by its corresponding elastic model (shown in the lower panes of Figure 11), so that the relative effect of thermo-viscoelasticity per geometry can be identified. Spherical reservoirs do not concentrate the applied stresses, and so sustain the greatest overpressures prior to failure (e.g., Currenti & Williams, 2014; Gerbault et al., 2018; Zhan & Gregg, 2019), with the normalized critical overpressures (Figure 11a) exceeding those of the oblate and prolate geometries. Like the spherical reservoir, the failure of an oblate reservoir (aspect ratio >1) is inhibited by the thermo-viscoelastic crust (Figure 11a), sustaining overpressures that are up to 35% greater than the elastic model. In contrast, prolate reservoir geometries (aspect ratio <1) demonstrate that a thermo-viscoelastic rheology can either hinder or promote reservoir failure, relative to the elastic model, depending on the reservoir temperature. Critical overpressures are increased by up to 15% for low-temperature reservoirs and decreased by up to 10% for high-temperature reservoirs (Figure 11a). Irrespective of the reservoir geometry, critical overpressures are maximized for low-temperature reservoirs when using a geothermal gradient of 30 K km^{-1}. Failure occurs at the lateral vertex for oblate reservoirs, and the apex for prolate reservoirs; the location of rupture along the reservoir wall does not vary with the imposed reservoir temperature, unlike the spherical geometry (Figure 7). As seen for the critical overpressure (Figure 11a), the spherical reservoir produces the greatest displacement relative to the elastic model at the time of failure (Figure 11b), with low reservoir temperatures producing increased deformation. A similar trend is shown for alternative geometries, although the variation with reservoir temperature is lower. Despite a few models requiring lower overpressures for failure, prolate reservoirs still produce elevated deformation within a thermo-viscoelastic crust, relative to the elastic model. We note that failure should initiate at the base of the prolate reservoir, with the region of localized tension (Figure 10f). Our models show that tensile failure subsequently occurs at the reservoir apex, which we have chosen to report here in Figure 11.

Prolate geometries deviate from the general trends identified throughout this study, with the capacity for thermo-viscoelasticity to promote reservoir failure. For high-temperature reservoirs, continued pressurization results in the emergence of a localized region of viscous tension at the reservoir apex (Figures S4 and S5 in Supporting Information S1) associated with geometric stress concentration, like that observed at the base of the reservoir (Figure 10f). This enables thermo-viscoelasticity to promote failure by increasing the local tensile stress, provided that the viscous timescales are sufficiently short. For a reservoir temperature of 900°C, viscous tension is not produced at the reservoir apex as the characteristic timescales are longer than the time taken for failure. Together, these results highlight an avenue for research and sensitivity testing to further explore the conditions that could promote reservoir failure, such as the roof thickness.
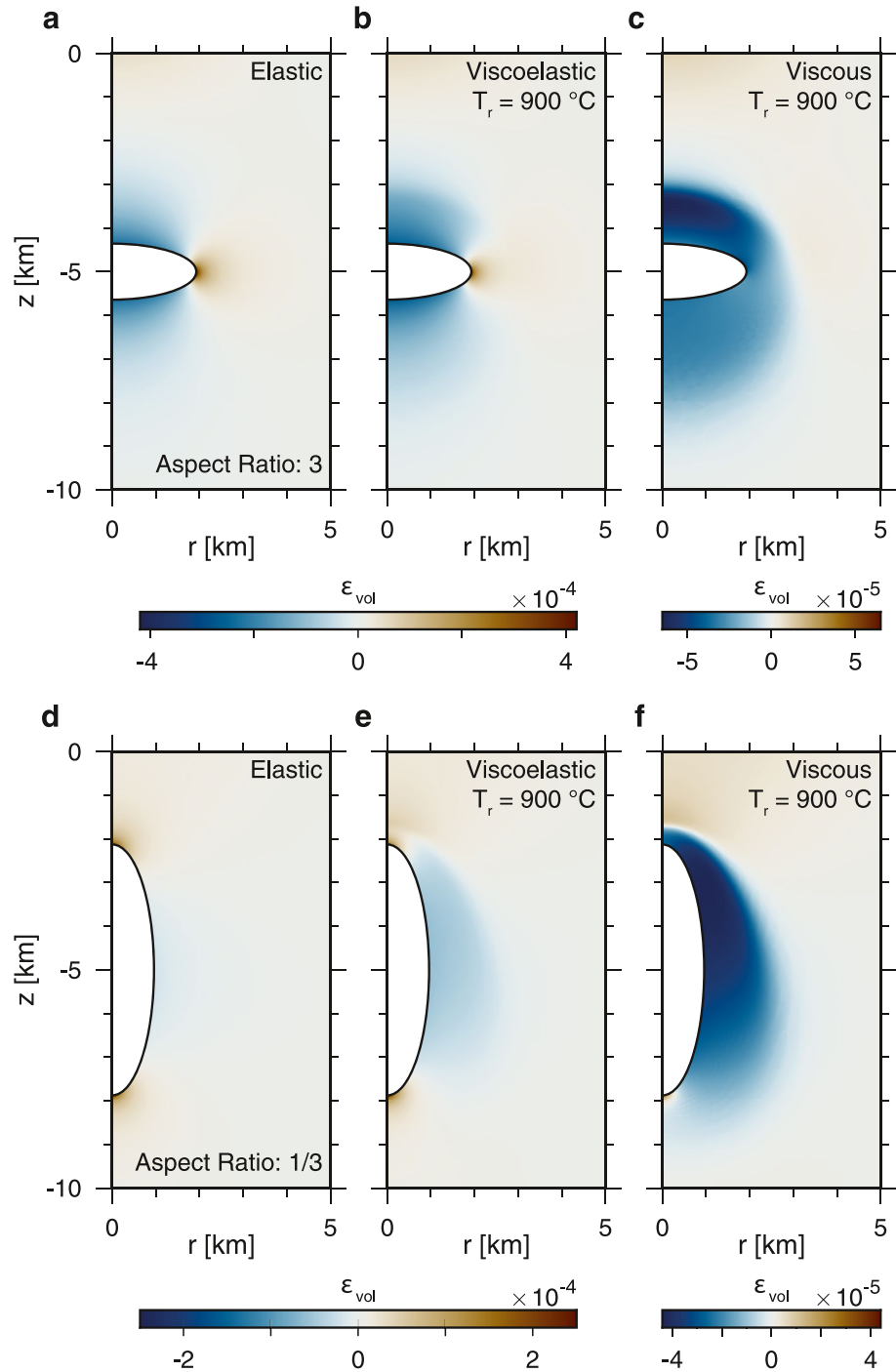
Figure 10. Partitioning of volumetric strain (ε_{vol}) and induced viscous compression for select oblate (a–c) and prolate (d–f) reservoir geometries in response to an overpressure loading rate of 1 MPa yr^{-1}. Cross-sections are evaluated at an overpressure of 10 MPa. Strain is concentrated at the reservoir vertices, unlike the spherical geometry (Figure 4), producing regions of relative tension and compression (a, b, d and e). Induced compression within the thermo-viscoelastic models can be identified when the component of viscous strain (c and f) is isolated, by removing the elastic strain (a and d) from the thermo-viscoelastic models (b and e). Compression due to non-uniform crustal viscosity is therefore applicable to all reservoir geometries.
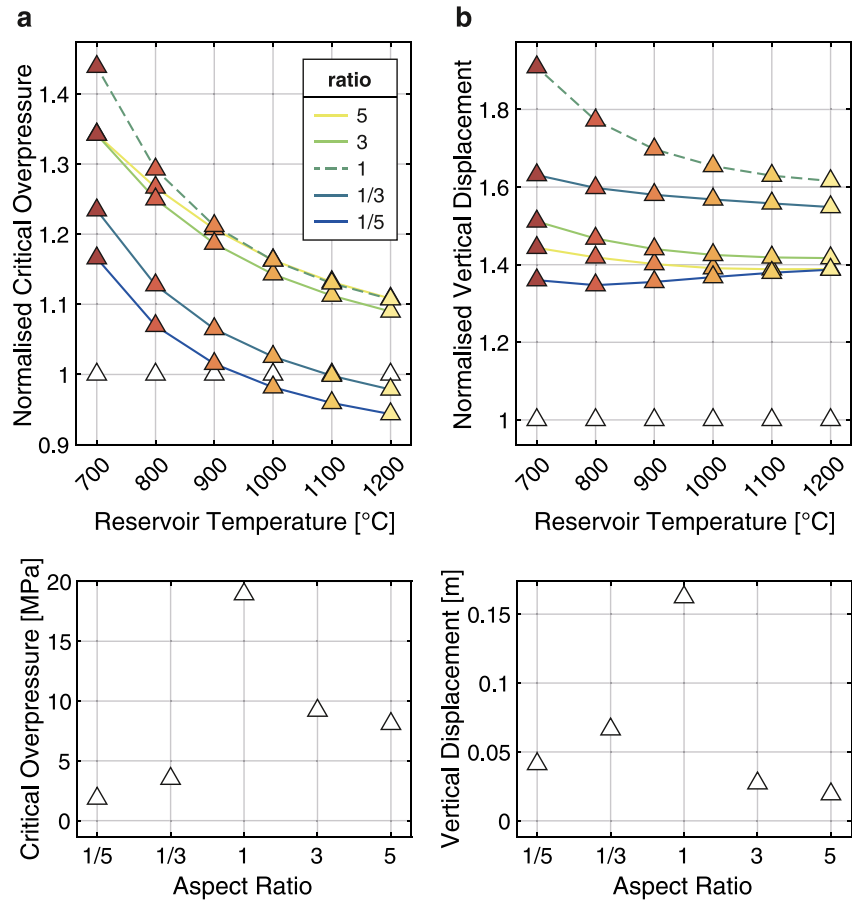
Figure 11. Impact of the reservoir geometry on tensile failure and ground deformation. Results are normalized by the elastic model for each geometry (shown in the lower panels), and the "base" model suite is indicated by a dashed trendline. (a) Overpressure required to initiate tensile failure on the reservoir wall. (b) Coincident vertical displacement at the ground surface ($r = z = 0$). Reservoir geometry is a key control on whether thermo-viscoelasticity acts to inhibit or promote brittle failure, with prolate geometries (ratio <1) capable of failing at lower overpressures relative to the elastic model. Critical overpressures are minimized for high-temperature reservoirs. Hollow markers depict elastic results, unaffected by the thermal conditions, whilst thermo-viscoelastic results are shown by solid markers, colored by reservoir temperature.

5. Implications and Limitations

Continued inflation of a magma reservoir within a thermo-viscoelastic crust induces an aureole of compression in the surrounding host-rock, due to the non-uniform crustal viscosity. This acts to resist mechanical failure along the reservoir wall; inhibiting the formation of magma-filled cracks and shear fractures. As such, a thermo-viscoelastic crust can enable deforming magmatic reservoirs to sustain elevated overpressures prior to failure, compared to elastic analyses. The compressive aureole, and associated strain-gradients, will likely also alter the propagation pathways of fractures, impacting the transportation of magma away from a ruptured magmatic system (e.g., Jellinek & DePaolo, 2003; Rubin, 1995) and volcano-tectonic seismicity, relating to the brittle failure of surrounding rock (Roman & Cashman, 2006).

When incorporating crustal viscoelasticity, the magmatic overpressures inferred from geodetic observations are typically of lower magnitude than those suggested by elastic models. Given the elevated overpressures required for mechanical failure and the reduced causative overpressures to reproduce observed deformation, the timescales for reservoir failure in a thermo-viscoelastic crust can greatly exceed those suggested by elastic analyses (e.g., Cabaniss et al., 2020). In the instance where the failure timescales of elastic analyses "fit" observations, additional processes that act to promote reservoir failure may need to be considered when using a thermo-viscoelastic rheology. This may include the presence of pre-existing weaknesses along the reservoir wall, additional stresses associated with magma buoyancy (e.g., Caricchi et al., 2014; Sigmundsson et al., 2020), or dynamic processes

during unrest such as cyclic loading, material fatigue and fracture healing (e.g., Cerfontaine & Collin, 2018; Kendrick et al., 2013; Lamur et al., 2019). External factors can increase the tensile stress around the reservoir, promoting failure, such as extensional tectonics (e.g., Cabaniss et al., 2018; Karaoğlu et al., 2020), regional earthquakes (e.g., Linde & Sacks, 1998; Manga & Brodsky, 2006) or localized pore pressure gradients (e.g., Rozhko et al., 2007).

5.1. Pore Fluid Pressure

There are different approaches when incorporating pore fluid pressure into failure analyses (e.g., Gerbault et al., 2012; Grosfils et al., 2015; Gudmundsson, 2012). A common approach assumes the presence of fluids within the host rock (Lister & Kerr, 1991; Rubin, 1995), adjacent to the reservoir, whereby the pore fluid pressure is equal to the lithostatic pressure. This results in the failure overpressure being of similar magnitude to the tensile or shear strength of the surrounding host rock (e.g., Gerbault et al., 2012, 2018; Gudmundsson, 2012). As such, this approach determines the minimum overpressure required for reservoir failure. Alternative analyses consider the role of horizontal pore pressure gradients and locally-induced gradients, and outline the impact on failure (e.g., Gerbault et al., 2012; Rozhko et al., 2007). Notably, the assumption of pore fluids adjacent to a reservoir (Lister & Kerr, 1991; Rubin, 1995) suggests porosity of the surrounding crustal rock, which has been shown to impact key physical properties of the rock (e.g., Heap et al., 2021; Heap & Violay, 2021). The degree of bedrock porosity (e.g., Gerbault et al., 2012) and permeability (e.g., Mittal & Richards, 2019), and the specific nature of the fluids are therefore important considerations for future failure analyses (e.g., Ruz-Ginouves et al., 2021). If instead the pore fluid pressure is assumed to be zero, as would be the case for dry host rock (e.g., Grosfils, 2007; Grosfils et al., 2015), then the overpressure required for reservoir failure is controlled by the lithostatic stress field. Gravitational loading puts the system into a compressive regime, requiring large values of overpressure to initiate either tensile or shear failure on the reservoir wall. It follows that the critical overpressure increases for reservoirs located at greater crustal depths (e.g., Albino et al., 2018; Grosfils, 2007; Zhan et al., 2019). The depth-dependent stress field associated with zero pore pressure can promote shear failure over tensile failure (e.g., Gerbault et al., 2012, 2018; Zhan & Gregg, 2019).

A non-zero pore fluid pressure encourages failure by decreasing the normal stress on the reservoir wall, shifting the Mohr circle closer toward the failure envelope (e.g., Rozhko et al., 2007). By balancing the pore pressure against the gravitational load, the assumption of lithostatic pore pressure produces conditions that are most favorable for brittle failure, minimizing the overpressures required. As the influence of thermo-viscoelasticity is shown to be prominent for favorable failure conditions, our findings are therefore applicable to alternative pore pressure conditions, which act to increase the overpressure requirements and lengthen the timescale of failure.

5.2. Physical Crustal Properties

Naturally, one of the greatest uncertainties when modeling reservoir failure lies in the knowledge of properties of the host rock surrounding the magmatic system (Zhan & Gregg, 2019). Recent laboratory studies have demonstrated that key physical parameters of volcanic rocks, such as Young's modulus and strength, are highly dependent on the porosity of the rock (Heap et al., 2020, 2021; Heap & Violay, 2021). Porous rocks at high confining pressures can undergo compaction, which may foster additional inelastic behavior. For simplicity, the role of host rock porosity was not accounted for in this study. Understanding how the strength of volcanic rocks (Heap & Violay, 2021) may vary at the depths of magma storage, and the role of material fatigue, where magmatic systems undergo overpressure cycling during unrest (e.g., Cerfontaine & Collin, 2018; Kendrick et al., 2013), are important considerations for models of reservoir failure. Further, several studies demonstrate that the physical properties of rocks are strongly controlled by temperature, such as the Young's modulus (e.g., Bakker et al., 2016; Balme et al., 2004; Smith et al., 2009), which can be incorporated into models of reservoir failure to account for thermal weakening of the host rock (e.g., Bakker et al., 2016; Cabaniss et al., 2020; Zhan et al., 2019). As the elastic deformation response is linearly related to the Young's modulus (c.f. Hooke's law), a similar compression effect would be observed in elastic models with heterogeneous mechanical parameters, such as a temperature-dependent Young's modulus which decreases in the vicinity of the modeled reservoir (e.g., Zhan et al., 2019). Combining a heterogeneous Young's modulus with a thermo-viscoelastic model could therefore result in an even greater impact on the induced tensile stress, further inhibiting failure (e.g., Cabaniss et al., 2020). Changing the tensile and shear strengths of the host-rock alters the absolute overpressures required for failure, but does not impact the

key results obtained; we show that crustal thermo-viscoelasticity impacts the onset of reservoir failure over a wide range of overpressure loading rates (Figure 8). These results can therefore be extended to studies using different material properties. Morales Rivera et al. (2019) demonstrate that the parameterization of crustal viscosity, to account for different crustal compositions, strongly affects the interpretations of volcanic ground deformation. Understanding how crustal viscosity can vary as a function of composition, temperature, water and silica content, etc., remains an important area for future study. Caution should therefore be exercised when defining model parameters, as the availability of data relating to different rock compositions is limited and the scaling of parameters from laboratory studies to crustal-scale applications is uncertain.

5.3. Modeling Considerations

Our model configuration contains several simplifications, including the assumption that the free surface above the magmatic system is flat; the work of Albino et al. (2018) demonstrates that failure overpressures can be significantly affected by including the topographic stress field due to a volcanic edifice. Failure analyses of island or submarine volcanoes should account for the ambient stress field due to the surrounding or overlying water mass, which also impacts the onset of reservoir failure (Cabaniss et al., 2020; Satow et al., 2021; Zhan et al., 2021). Additionally, the models used here assume that the crustal rock is competent and does not contain pre-existing fractures, therefore neglecting the role of pre-existing weaknesses along or near to the reservoir wall, which can act to reduce failure thresholds for both elastic and thermo-viscoelastic models, or govern where such failure may predominantly occur. Furthermore, in this study we neglect the role of magma injection by applying an overpressure directly to the reservoir wall, and therefore our models do not account for the relationship between reservoir pressurization and the fluxes and timescales associated with injection (e.g., Degruyter & Huber, 2014; Gregg et al., 2018; Le Mével et al., 2016; Townsend et al., 2019). While our results are insightful for failure analyses within a thermo-viscoelastic crust, incorporating these physical mechanisms and cyclical internal dynamics to provide a robust comparison with alternative modeling approaches (e.g., Degruyter & Huber, 2014; Jellinek & DePaolo, 2003; Karlstrom et al., 2010; Mittal & Richards, 2019; Townsend et al., 2019) will likely improve the understanding of unrest processes and reservoir failure.

Primarily, this study demonstrates that crustal thermo-viscoelasticity generally enables hotter, less-viscous wall rock to fracture at lower overpressures than cooler, more-viscous rock. This could indicate that, in nature, there are additional rheological effects at play that the Standard Linear Solid thermo-viscoelastic rheology cannot account for, and is therefore unlikely to provide a complete representation for the behavior of the entire crustal column. Such effects may also include poroelasticity (e.g., Liao et al., 2018, 2021), elastoplasticity (e.g., Currenti & Williams, 2014; Gerbault et al., 2012; Got et al., 2013), alternative rheological models (e.g., Burgers viscoelasticity), or likely a complex combination of several behaviors (e.g., Burov, 2011). Incorporating additional rheological effects within numerical models will provide further insight into the conditions required for volcanic eruptions, helping to understand the competition between the loading and failure rates in the presence of time-dependent rheological processes, whilst also sensitive to local thermal and chemical variations. Although field observations show that rock surrounding magmatic systems undergo predominantly brittle failure, as evidenced by the presence of fractures (Gudmundsson, 2020), this study may further highlight the requirement for dynamic failure criteria that explicitly account for strain-rate, such that viscous material can still fail in a brittle fashion given a sufficiently high strain-rate. Studies of deforming magma use dynamic failure criteria (e.g., Dingwell, 1996; Gottsmann et al., 2009), whereby strain-rate is a primary control on the transition to solid-like behavior. Strain-rate dependence should be more widely explored and applied to reservoir failure analyses during episodes of unrest (Gottsmann et al., 2009; Gottsmann & Odbert, 2014), particularly when incorporating inelastic crustal behavior. Fundamentally, our results highlight the requirement for further laboratory testing of crustal rocks at confining pressures and temperatures representative of magma storage to better understand the range of potential rheological effects and conditions for failure, informing future numerical models. However, adequately relating laboratory-scale measurements to crustal-scale applications remains an ever-present consideration and challenge for thermomechanical analyses.

6. Conclusions

Thermo-viscoelasticity is increasingly utilized in models of ground deformation, accounting for the induced thermomechanical heterogeneity (e.g., Hickey et al., 2016; Le Mével et al., 2016). However, outside of the effect on surface deformation, the impacts of varying rheology on other physical processes occurring at depth remain comparatively poorly explored (Cabaniss et al., 2020; Gottsmann & Odbert, 2014; Gregg et al., 2012). Here, we address this research-gap by systematically investigating the failure of a pressurizing magmatic system within a thermo-viscoelastic crust and identifying the controlling processes. Our results demonstrate that the thermo-viscoelastic rheology allows a deforming magmatic system to sustain greater overpressures relative to the elastic model, inhibiting brittle failure. The relative overpressures are strongly influenced by the imposed thermal constraints (i.e., reservoir temperature and geothermal gradient), rate of overpressure loading, and reservoir geometry. Reservoir temperature is a primary control on failure; low-temperature reservoirs exhibit the greatest critical overpressures, which decrease for increased reservoir temperatures. We illustrate that, fundamentally, it is the difference between the viscous timescales of hotter rocks of reduced viscosity, close to the reservoir, and cooler crustal material of greater viscosity, away from the reservoir, that allows the deforming reservoir to sustain elevated overpressures prior to failure. This effect arises due to an inherent lag in viscous timescales, so does not occur in media of uniform viscosity. As such, failure analyses should not neglect the role of thermo-viscoelasticity.

Given that thermo-viscoelasticity generally resists the mechanical failure of a deforming reservoir, impacting the conditions required to nucleate magma-filled cracks and form shear fractures, this phenomenon is consistent with the many observed episodes of ground deformation not followed by an eruption (e.g., Biggs et al., 2014; Le Mével et al., 2021; Parks et al., 2015). However, greater focus may then be placed on alternative processes that act to promote reservoir failure, including the role of material fatigue and cyclic loading, internal forces (e.g., buoyancy), regional stresses (e.g., topographic, and tectonic), geometric stress concentration, external triggers (e.g., earthquake stress drops), or pre-existing weaknesses or irregularities along the reservoir wall. Furthermore, understanding how key physical parameters of crustal and volcanic rocks (Heap & Violay, 2021) may vary at the temperatures and pressures typical of magma storage is crucial for reducing sources of uncertainty (e.g., tensile and shear strengths) in reservoir failure models. Ultimately, this study highlights the role of an assumed crustal rheology and the importance of accurate thermal constraints and material properties, including those in the calculation of crustal viscosity, which directly impact the timing of reservoir failure.

Data Availability Statement

Numerical modelling was carried out using COMSOL Multiphysics® (https://uk.comsol.com); data were not used nor created for this research.

References

Acocella, V., Di Lorenzo, R., Newhall, C., & Scandone, R. (2015). An overview of recent (1988 to 2014) caldera unrest: Knowledge and perspectives. *Reviews of Geophysics*, *53*(3), 896–955. https://doi.org/10.1002/2015RG000492

Albino, F., Amelung, F., & Gregg, P. M. (2018). The role of pore fluid pressure on the failure of magma reservoirs: Insights from Indonesian and Aleutian Arc volcanoes. *Journal of Geophysical Research: Solid Earth*, *123*(2), 1328–1349. https://doi.org/10.1002/2017JB014523

Albino, F., Pinel, V., & Sigmundsson, F. (2010). Influence of surface load variations on eruption likelihood: Application to two Icelandic subglacial volcanoes, Grímsvötn and Katla. *Geophysical Journal International*, *181*, 1510–1524. https://doi.org/10.1111/j.1365-246X.2010.04603.x

Albright, J. A., Gregg, P. M., Lu, Z., & Freymueller, J. T. (2019). Hindcasting magma reservoir stability preceding the 2008 eruption of Okmok, Alaska. *Geophysical Research Letters*, *46*(15), 8801–8808. https://doi.org/10.1029/2019GL083395

Annen, C. (2011). Implications of incremental emplacement of magma bodies for magma differentiation, thermal aureole dimensions and Plutonism–volcanism relationships. *Tectonophysics*, *500*(1–4), 3–10. https://doi.org/10.1016/j.tecto.2009.04.010

Bakker, R. R., Frehner, M., & Lupi, M. (2016). How temperature-dependent elasticity alters host rock/magmatic reservoir models: A case study on the effects of ice-cap unloading on shallow volcanic systems. *Earth and Planetary Science Letters*, *456*, 16–25. https://doi.org/10.1016/j.epsl.2016.09.039

Balme, M. R., Rocchi, V., Jones, C., Sammonds, P. R., Meredith, P. G., & Boon, S. (2004). Fracture toughness measurements on igneous rocks using a high-pressure, high-temperature rock fracture mechanics cell. *Journal of Volcanology and Geothermal Research*, *132*(2–3), 159–172. https://doi.org/10.1016/S0377-0273(03)00343-3

Banks, H. T., Hu, S., & Kenz, Z. R. (2011). A brief review of elasticity and viscoelasticity for solids. *Advances in Applied Mathematics and Mechanics*, *3*(1), 1–51. https://doi.org/10.4208/aamm.10-m1030

Barton, N., & Choubey, V. (1977). The shear strength of rock joints in theory and practice. *Rock Mechanics*, *10*(1–2), 1–54. https://doi.org/10.1007/BF01261801

Bato, M. G., Pinel, V., & Yan, Y. (2017). Assimilation of deformation data for eruption forecasting: Potentiality assessment based on synthetic cases. *Frontiers of Earth Science*, *5*, 1–23. https://doi.org/10.3389/feart.2017.00048

Biggs, J., Ebmeier, S. K., Aspinall, W. P., Lu, Z., Pritchard, M. E., Sparks, R. S. J., & Mather, T. A. (2014). Global link between deformation and volcanic eruption quantified by satellite imagery. *Nature Communications*, *5*(1), 3471. https://doi.org/10.1038/ncomms4471

Biggs, J., & Pritchard, M. E. (2017). Global volcano monitoring: What does it mean when volcanoes deform? *Elements*, *13*(1), 17–22. https://doi.org/10.2113/gselements.13.1.17

Browning, J., Drymoni, K., & Gudmundsson, A. (2015). Forecasting magma-chamber rupture at Santorini volcano, Greece. *Scientific Reports*, *5*(1), 15785. https://doi.org/10.1038/srep15785

Browning, J., Karaoğlu, Ö., Bayer, Ö., Turgay, M. B., & Acocella, V. (2021). Stress fields around magma chambers influenced by elastic thermo-mechanical deformation: Implications for forecasting chamber failure. *Bulletin of Volcanology*, *83*(7), 48. https://doi.org/10.1007/s00445-021-01471-2

Burov, E. B. (2011). Rheology and strength of the lithosphere. *Marine and Petroleum Geology*, *28*(8), 1402–1443. https://doi.org/10.1016/j.marpetgeo.2011.05.008

Cabaniss, H. E., Gregg, P. M., & Grosfils, E. B. (2018). The role of tectonic stress in triggering large silicic caldera eruptions. *Geophysical Research Letters*, *45*(9), 3889–3895. https://doi.org/10.1029/2018GL077393

Cabaniss, H. E., Gregg, P. M., Nooner, S. L., & Chadwick, W. W. (2020). Triggering of eruptions at axial seamount, Juan de Fuca ridge. *Scientific Reports*, *10*(1), 10219. https://doi.org/10.1038/s41598-020-67043-0

Caricchi, L., Annen, C., Blundy, J., Simpson, G., & Pinel, V. (2014). Frequency and magnitude of volcanic eruptions controlled by magma injection and buoyancy. *Nature Geoscience*, *7*(2), 126–130. https://doi.org/10.1038/ngeo2041

Cerfontaine, B., & Collin, F. (2018). Cyclic and fatigue behaviour of rock materials: Review, interpretation and research perspectives. *Rock Mechanics and Rock Engineering*, *51*(2), 391–414. https://doi.org/10.1007/s00603-017-1337-5

Christensen, R. M. (1982). *Theory of viscoelasticity: An introduction*. Dover Publications.

Crameri, F. (2018). Scientific colour Maps. *Zenodo*. https://doi.org/10.5281/zenodo.1243862

Crawford, R. J. (1998). *Plastics engineering*. Butterworth-Heinemann.

Currenti, G. (2018). Viscoelastic modeling of deformation and gravity changes induced by pressurized magmatic sources. *Journal of Volcanology and Geothermal Research*, *356*, 264–277. https://doi.org/10.1016/j.jvolgeores.2018.03.020

Currenti, G., Bonaccorso, A., Del Negro, C., Scandura, D., & Boschi, E. (2010). Elasto-plastic modeling of volcano ground deformation. *Earth and Planetary Science Letters*, *296*, (3–4), 311–318. https://doi.org/10.1016/j.epsl.2010.05.013

Currenti, G., & Williams, C. A. (2014). Numerical modeling of deformation and stress fields around a magma chamber: Constraints on failure conditions and rheology. *Physics of the Earth and Planetary Interiors*, *226*, 14–27. https://doi.org/10.1016/j.pepi.2013.11.003

Dahm, T. (2000). Numerical simulations of the propagation path and the arrest of fluid-filled fractures in the Earth. *Geophysical Journal International*, *141*(3), 623–638. https://doi.org/10.1046/j.1365-246X.2000.00102.x

de Silva, S. L., & Gregg, P. M. (2014). Thermomechanical feedbacks in magmatic systems: Implications for growth, longevity, and evolution of large caldera-forming magma reservoirs and their supereruptions. *Journal of Volcanology and Geothermal Research*, *282*, 77–91. https://doi.org/10.1016/j.jvolgeores.2014.06.001

Degruyter, W., & Huber, C. (2014). A model for eruption frequency of upper crustal silicic magma chambers. *Earth and Planetary Science Letters*, *403*, 117–130. https://doi.org/10.1016/j.epsl.2014.06.047

Del Negro, C., Currenti, G., & Scandura, D. (2009). Temperature-dependent viscoelastic modeling of ground deformation: Application to Etna volcano during the 1993–1997 inflation period. *Physics of the Earth and Planetary Interiors*, *172*(3–4), 299–309. https://doi.org/10.1016/j.pepi.2008.10.019

Dingwell, D. B. (1996). Volcanic Dilemma: Flow or blow? *Science*, *273*(5278), 1054–1055. https://doi.org/10.1126/science.273.5278.1054

Dragoni, M., & Magnanensi, C. (1989). Displacement and stress produced by a pressurized, spherical magma chamber, surrounded by a viscoelastic shell. *Physics of the Earth and Planetary Interiors*, *56*(3–4), 316–328. https://doi.org/10.1016/0031-9201(89)90166-0

Ebmeier, S. K., Andrews, B. J., Araya, M. C., Arnold, D. W. D., Biggs, J., Cooper, C., et al. (2018). Synthesis of global satellite observations of magmatic and volcanic deformation: Implications for volcano monitoring & the lateral extent of magmatic domains. *Journal of Applied Volcanology*, *7*(1), 1–26. https://doi.org/10.1186/s13617-018-0071-3

Folch, A., Fernández, J., Rundle, J. B., & Martí, J. (2000). Ground deformation in a viscoelastic medium composed of a layer overlying a half-space: A comparison between point and extended sources. *Geophysical Journal International*, *140*(1), 37–50. https://doi.org/10.1046/j.1365-246x.2000.00003.x

Fung, Y. C. (1965). *Foundations of solid mechanics*, Prentice-Hall.

Fung, Y. C. (1969). *A first course in continuum mechanics*, Prentice-Hall.

Gelman, S. E., Gutiérrez, F. J., & Bachmann, O. (2013). On the longevity of large upper crustal silicic magma reservoirs. *Geology*, *41*(7), 759–762. https://doi.org/10.1130/G34241.1

Gerbault, M., Cappa, F., & Hassani, R. (2012). Elasto-plastic and hydromechanical models of failure around an infinitely long magma chamber. *Geochemistry, Geophysics, Geosystems*, *13*(3). https://doi.org/10.1029/2011GC003917

Gerbault, M., Hassani, R., Novoa Lizama, C., & Souche, A. (2018). Three-dimensional failure patterns around an inflating magmatic chamber. *Geochemistry, Geophysics, Geosystems*, *19*(3), 749–771. https://doi.org/10.1002/2017GC007174

Got, J.-L., Peltier, A., Staudacher, T., Kowalski, P., & Boissier, P. (2013). Edifice strength and magma transfer modulation at Piton de la Fournaise Volcano. *Journal of Geophysical Research: Solid Earth*, *118*(9), 5040–5057. https://doi.org/10.1002/jgrb.50350

Gottsmann, J., Blundy, J., Henderson, S., Pritchard, M. E., & Sparks, R. S. J. (2017). Thermomechanical modeling of the Altiplano-Puna deformation anomaly: Multiparameter insights into magma mush reorganization. *Geosphere*, *13*, GES01420. https://doi.org/10.1130/GES01420.1

Gottsmann, J., Lavallée, Y., Martí, J., & Aguirre-díaz, G. (2009). Magma-tectonic interaction and the eruption of silicic batholiths. *Earth and Planetary Science Letters*, *284*(3–4), 426–434. https://doi.org/10.1016/j.epsl.2009.05.008

Gottsmann, J., & Odbert, H. (2014). The effects of thermomechanical heterogeneities in island arc crust on time-dependent preeruptive stresses and the failure of an andesitic reservoir. *Journal of Geophysical Research: Solid Earth*, *119*(6), 4626–4639. https://doi.org/10.1002/2014JB011079

Gregg, P. M., de Silva, S. L., & Grosfils, E. B. (2013). Thermomechanics of shallow magma chamber pressurization: Implications for the assessment of ground deformation data at active volcanoes. *Earth and Planetary Science Letters*, *384*, 100–108. https://doi.org/10.1016/j.epsl.2013.09.040

Gregg, P. M., de Silva, S. L., Grosfils, E. B., & Parmigiani, J. P. (2012). Catastrophic caldera-forming eruptions: Thermomechanics and implications for eruption triggering and maximum caldera dimensions on Earth. *Journal of Volcanology and Geothermal Research*, *241–242*, 1–12. https://doi.org/10.1016/j.jvolgeores.2012.06.009

Gregg, P. M., Le Mével, H., Zhan, Y., Dufek, J., Geist, D., & Chadwick, W. W. (2018). Stress triggering of the 2005 eruption of Sierra Negra Volcano, Galápagos. *Geophysical Research Letters*, *45*(24), 13288–13297. https://doi.org/10.1029/2018GL080393

Grosfils, E. B. (2007). Magma reservoir failure on the terrestrial planets: Assessing the importance of gravitational loading in simple elastic models. *Journal of Volcanology and Geothermal Research*, *166*(2), 47–75. https://doi.org/10.1016/j.jvolgeores.2007.06.007

Grosfils, E. B., McGovern, P. J., Gregg, P. M., Galgana, G. A., Hurwitz, D. M., Long, S. M., & Chestler, S. R. (2015). Elastic models of magma reservoir mechanics: A key tool for investigating planetary volcanism. In T. Platz, M. Massironi, P. K. Byrne, & H. Hiesinger (Eds.), *Volcanism and tectonism across the inner solar system* (Vol. 401(1), pp. 239–267). Geological Society, London, Special Publications. https://doi.org/10.1144/SP401.2

Gudmundsson, A. (2006). How local stresses control magma-chamber ruptures, dyke injections, and eruptions in composite volcanoes. *Earth-Science Reviews*, *79*(1–2), 1–31. https://doi.org/10.1016/j.earscirev.2006.06.006

Gudmundsson, A. (2011). *Rock fractures in geological processes*. Cambridge University Press.

Gudmundsson, A. (2012). Magma chambers: Formation, local stresses, excess pressures, and compartments. *Journal of Volcanology and Geothermal Research*, *237–238*, 19–41. https://doi.org/10.1016/j.jvolgeores.2012.05.015

Gudmundsson, A. (2020). *Volcanotectonics*, Cambridge University Press. https://doi.org/10.1017/9781139176217

Head, M., Hickey, J., Gottsmann, J., & Fournier, N. (2019). The influence of viscoelastic crustal Rheologies on volcanic ground deformation: Insights from models of pressure and volume change. *Journal of Geophysical Research: Solid Earth*, *124*(8), 8127–8146. https://doi.org/10.1029/2019JB017832

Head, M., Hickey, J., Gottsmann, J., & Fournier, N. (2021). Exploring the impact of thermally controlled crustal viscosity on volcanic ground deformation. *Journal of Geophysical Research: Solid Earth*, *126*(8), 1–22. https://doi.org/10.1029/2020JB020724

Heap, M. J., Villeneuve, M., Albino, F., Farquharson, J. I., Brothelande, E., Amelung, F., et al. (2020). Towards more realistic values of elastic moduli for volcano modelling. *Journal of Volcanology and Geothermal Research*, *390*, 106684. https://doi.org/10.1016/j.jvolgeores.2019.106684

Heap, M. J., & Violay, M. E. S. (2021). The mechanical behaviour and failure modes of volcanic rocks: A review. *Bulletin of Volcanology*, *83*(5), 33. https://doi.org/10.1007/s00445-021-01447-2

Heap, M. J., Wadsworth, F. B., Heng, Z., Xu, T., Griffiths, L., Aguilar Velasco, A., et al. (2021). The tensile strength of volcanic rocks: Experiments and models. *Journal of Volcanology and Geothermal Research*, *418*, 107348. https://doi.org/10.1016/j.jvolgeores.2021.107348

Hickey, J., & Gottsmann, J. (2014). Benchmarking and developing numerical Finite Element models of volcanic deformation. *Journal of Volcanology and Geothermal Research*, *280*, 126–130. https://doi.org/10.1016/j.jvolgeores.2014.05.011

Hickey, J., Gottsmann, J., & Mothes, P. (2015). Estimating volcanic deformation source parameters with a finite element inversion: The 2001–2002 unrest at Cotopaxi volcano, Ecuador. *Journal of Geophysical Research: Solid Earth*, *120*(3), 1473–1486. https://doi.org/10.1002/2014JB011731

Hickey, J., Gottsmann, J., Nakamichi, H., & Iguchi, M. (2016). Thermomechanical controls on magma supply and volcanic deformation: Application to Aira Caldera, Japan. *Scientific Reports*, *6*(1), 32691. https://doi.org/10.1038/srep32691

Holohan, E. P., Sudhaus, H., Walter, T. R., Schöpfer, M. P. J., & Walsh, J. J. (2017). Effects of host-rock fracturing on elastic-deformation source models of volcano deflation. *Scientific Reports*, *7*(1), 1–12. https://doi.org/10.1038/s41598-017-10009-6

Jaeger, J. C., Cook, N. G. W., & Zimmerman, R. (2007). *Fundamentals of rock mechanics*, Blackwell.

Jellinek, A. M., & DePaolo, D. J. (2003). A model for the origin of large silicic magma chambers: Precursors of caldera-forming eruptions. *Bulletin of Volcanology*, *65*(5), 363–381. https://doi.org/10.1007/s00445-003-0277-y

Karakas, O., Degruyter, W., Bachmann, O., & Dufek, J. (2017). Lifetime and size of shallow magma bodies controlled by crustal-scale magmatism. *Nature Geoscience*, *10*(6), 446–450. https://doi.org/10.1038/ngeo2959

Karaoğlu, Ö., Bayer, Ö., Turgay, M. B., & Browning, J. (2020). Thermomechanical interactions between crustal magma chambers in complex tectonic environments: Insights from Eastern Turkey. *Tectonophysics*, *793*, 228607. https://doi.org/10.1016/j.tecto.2020.228607

Karlstrom, L., Dufek, J., & Manga, M. (2010). Magma chamber stability in arc and continental crust. *Journal of Volcanology and Geothermal Research*, *190*(3–4), 249–270. https://doi.org/10.1016/j.jvolgeores.2009.10.003

Karlstrom, L., Paterson, S. R., & Jellinek, A. M. (2017). A reverse energy cascade for crustal magma transport. *Nature Geoscience*, *10*(8), 604–608. https://doi.org/10.1038/NGEO2982

Kavanagh, J. L., Engwell, S. L., & Martin, S. A. (2018). A review of laboratory and numerical modelling in volcanology. *Solid Earth*, *9*(2), 531–571. https://doi.org/10.5194/se-9-531-2018

Kendrick, J. E., Smith, R., Sammonds, P., Meredith, P. G., Dainty, M., & Pallister, J. S. (2013). The influence of thermal and cyclic stressing on the strength of rocks from Mount St. Helens, Washington. *Bulletin of Volcanology*, *75*(7), 728. https://doi.org/10.1007/s00445-013-0728-z

Lamur, A., Kendrick, J. E., Wadsworth, F. B., & Lavallée, Y. (2019). Fracture healing and strength recovery in magmatic liquids. *Geology*, *47*(3), 195–198. https://doi.org/10.1130/G45512.1

Le Mével, H., Córdova, L., Cardona, C., & Feigl, K. L. (2021). Unrest at the Laguna del Maule volcanic field 2005–2020: Renewed acceleration of deformation. *Bulletin of Volcanology*, *83*(6), 39. https://doi.org/10.1007/s00445-021-01457-0

Le Mével, H., Gregg, P. M., & Feigl, K. L. (2016). Magma injection into a long-lived reservoir to explain geodetically measured uplift: Application to the 2007–2014 unrest episode at Laguna del Maule volcanic field, Chile. *Journal of Geophysical Research: Solid Earth*, *121*(8), 6092–6108. https://doi.org/10.1002/2016JB013066

Lerner, A. H., O'Hara, D., Karlstrom, L., Ebmeier, S. K., Anderson, K. R., & Hurwitz, S. (2020). The prevalence and significance of offset magma reservoirs at Arc volcanoes. *Geophysical Research Letters*, *47*(14), 1–10. https://doi.org/10.1029/2020GL087856

Liao, Y., Soule, S. A., & Jones, M. (2018). On the mechanical effects of poroelastic crystal mush in classical magma chamber models. *Journal of Geophysical Research: Solid Earth*, *123*(11), 9376–9406. https://doi.org/10.1029/2018JB015985

Liao, Y., Soule, S. A., Jones, M., & Le Mével, H. (2021). The mechanical response of a magma chamber with poroviscoelastic crystal mush. *Journal of Geophysical Research: Solid Earth*, *126*(4), 1–19. https://doi.org/10.1029/2020JB019395

Linde, A. T., & Sacks, I. S. (1998). Triggering of volcanic eruptions. *Nature*, *395*(6705), 888–890. https://doi.org/10.1038/27650

Lister, J. R., & Kerr, R. C. (1991). Fluid-mechanical models of crack propagation and their application to magma transport in dykes. *Journal of Geophysical Research*, *96*(B6), 10049. https://doi.org/10.1029/91JB00600

Long, S. M., & Grosfils, E. B. (2009). Modeling the effect of layered volcanic material on magma reservoir failure and associated deformation, with application to Long Valley Caldera, California. *Journal of Volcanology and Geothermal Research*, *186*(3–4), 349–360. https://doi.org/10.1016/j.jvolgeores.2009.05.021

Lundgren, P., Girona, T., Bato, M. G., Realmuto, V. J., Samsonov, S., Cardona, C., et al. (2020). The dynamics of large silicic systems from satellite remote sensing observations: The intriguing case of Domuyo Volcano, Argentina. *Scientific Reports*, *10*(1), 1–15. https://doi.org/10.1038/s41598-020-67982-8

Manga, M., & Brodsky, E. (2006). Seismic triggering of eruptions in the far field: Volcanoes and Geysers. *Annual Review of Earth and Planetary Sciences*, *34*(1), 263–291. https://doi.org/10.1146/annurev.earth.34.031405.125125

Marques, S. P. C., & Creus, G. J. (2012). *Computational viscoelasticity*, Springer Berlin Heidelberg. https://doi.org/10.1007/978-3-642-25311-9

Masterlark, T., Haney, M., Dickinson, H., Fournier, T., & Searcy, C. (2010). Rheologic and structural controls on the deformation of Okmok Volcano, Alaska: FEMs, InSAR, and ambient noise tomography. *Journal of Geophysical Research*, *115*(B2), B02409. https://doi.org/10.1029/2009JB006324

McTigue, D. F. (1987). Elastic stress and deformation near a finite spherical magma body: Resolution of the point source paradox. *Journal of Geophysical Research*, *92*(B12), 12931. https://doi.org/10.1029/JB092iB12p12931

Meissner, R., & Tanner, B. (1992). Crustal viscosities and seismic velocities. *Physics of the Earth and Planetary Interiors*, *69*(3–4), 252–256. https://doi.org/10.1016/0031-9201(92)90143-J

Mittal, T., & Richards, M. A. (2019). Volatile Degassing from magma chambers as a control on volcanic eruptions. *Journal of Geophysical Research: Solid Earth*, *124*(8), 7869–7901. https://doi.org/10.1029/2018JB016983

Morales Rivera, A. M., Amelung, F., Albino, F., & Gregg, P. M. (2019). Impact of crustal rheology on temperature-dependent viscoelastic models of volcano deformation: Application to Taal Volcano, Philippines. *Journal of Geophysical Research: Solid Earth*, *124*(1), 978–994. https://doi.org/10.1029/2018JB016054

Newman, A. V., Dixon, T. H., & Gourmelen, N. (2006). A four-dimensional viscoelastic deformation model for Long Valley Caldera, California, between 1995 and 2000. *Journal of Volcanology and Geothermal Research*, *150*(1–3), 244–269. https://doi.org/10.1016/j.jvolgeores.2005.07.017

Newman, A. V., Dixon, T. H., Ofoegbu, G. I., & Dixon, J. E. (2001). Geodetic and seismic constraints on recent activity at long valley caldera, California: Evidence for viscoelastic rheology. *Journal of Volcanology and Geothermal Research*, *105*(3), 183–206. https://doi.org/10.1016/S0377-0273(00)00255-9

O'Connell, R. J., & Budiansky, B. (1977). Viscoelastic properties of fluid-saturated cracked solids. *Journal of Geophysical Research*, *82*(36), 5719–5735. https://doi.org/10.1029/JB082i036p05719

Parks, M. M., Moore, J. D. P., Papanikolaou, X., Biggs, J., Mather, T. A., Pyle, D. M., et al. (2015). From quiescence to unrest: 20 years of satellite geodetic measurements at Santorini Volcano, Greece. *Journal of Geophysical Research: Solid Earth*, *120*(2), 1309–1328. https://doi.org/10.1002/2014JB011540

Phillipson, G., Sobradelo, R., & Gottsmann, J. (2013). Global volcanic unrest in the 21st century: An analysis of the first decade. *Journal of Volcanology and Geothermal Research*, *264*, 183–196. https://doi.org/10.1016/j.jvolgeores.2013.08.004

Ranalli, G. (1995). *Rheology of the Earth*, Chapman and Hall.

Roman, D. C., & Cashman, K. V. (2006). The origin of volcano-tectonic earthquake swarms. *Geology*, *34*(6), 457. https://doi.org/10.1130/G22269.1

Rozhko, A. Y., Podladchikov, Y. Y., & Renard, F. (2007). Failure patterns caused by localized rise in pore-fluid overpressure and effective strength of rocks. *Geophysical Research Letters*, *34*(22), L22304. https://doi.org/10.1029/2007GL031696

Rubin, A. M. (1993). Dikes vs. diapirs in viscoelastic rock. *Earth and Planetary Science Letters*, *119*(4), 641–659. https://doi.org/10.1016/0012-821X(93)90069-L

Rubin, A. M. (1995). Propagation of magma-filled cracks. *Annual Review of Earth and Planetary Sciences*, *23*(1), 287–336. https://doi.org/10.1146/annurev.ea.23.050195.001443

Rucker, C., Erickson, B. A., Karlstrom, L., Lee, B., & Gopalakrishnan, J. (2022). A computational framework for time dependent deformation in viscoelastic magmatic systems. *EarthArXiv*. https://doi.org/10.31223/X5WH0N

Ruz-Ginouves, J., Gerbault, M., Cembrano, J., Iturrieta, P., Sáez Leiva, F., Novoa, C., & Hassani, R. (2021). The interplay of a fault zone and a volcanic reservoir from 3D elasto-plastic models: Rheological conditions for mutual trigger based on a field case from the Andean Southern Volcanic Zone. *Journal of Volcanology and Geothermal Research*, *418*, 107317. https://doi.org/10.1016/j.jvolgeores.2021.107317

Satow, C., Gudmundsson, A., Gertisser, R., Ramsey, C. B., Bazargan, M., Pyle, D. M., et al. (2021). Eruptive activity of the Santorini Volcano controlled by sea-level rise and fall. *Nature Geoscience*, *14*(8), 586–592. https://doi.org/10.1038/s41561-021-00783-4

Schutt, D. L., Lowry, A. R., & Buehler, J. S. (2018). Moho temperature and mobility of lower crust in the Western United States. *Geology*, *46*(3), 219–222. https://doi.org/10.1130/G39507.1

Segall, P. (2010). *Earthquake and volcano deformation*. Princeton University Press.

Sigmundsson, F., Pinel, V., Grapenthin, R., Hooper, A., Halldórsson, S. A., Einarsson, P., et al. (2020). Unexpected large eruptions from buoyant magma bodies within viscoelastic crust. *Nature Communications*, *11*(1), 2403. https://doi.org/10.1038/s41467-020-16054-6

Smith, R., Sammonds, P. R., & Kilburn, C. R. J. (2009). Fracturing of volcanic systems: Experimental insights into pre-eruptive conditions. *Earth and Planetary Science Letters*, *280*(1–4), 211–219. https://doi.org/10.1016/j.epsl.2009.01.032

Sparks, R. S. J., Biggs, J., & Neuberg, J. W. (2012). Monitoring volcanoes. *Science*, *335*(6074), 1310–1311. https://doi.org/10.1126/science.1219485

Sparks, R. S. J., & Cashman, K. V. (2017). Dynamic magma systems: Implications for forecasting volcanic activity. *Elements*, *13*(1), 35–40. https://doi.org/10.2113/gselements.13.1.35

Tait, S., Jaupart, C., & Vergniolle, S. (1989). Pressure, gas content and eruption periodicity of a shallow, crystallising magma chamber. *Earth and Planetary Science Letters*, *92*(1), 107–123. https://doi.org/10.1016/0012-821X(89)90025-3

Tilling, R. I. (2008). The critical role of volcano monitoring in risk reduction. *Advances in Geosciences*, *14*, 3–11. https://doi.org/10.5194/adgeo-14-3-2008

Townsend, M., Huber, C., Degruyter, W., & Bachmann, O. (2019). Magma chamber growth during inter-caldera periods: Insights from thermo-mechanical modeling with applications to Laguna del Maule, Campi Flegrei, Santorini, and Aso. *Geochemistry, Geophysics, Geosystems*, *20*(3), 1–18. https://doi.org/10.1029/2018GC008103

Wessel, P., Smith, W. H. F., Scharroo, R., Luis, J., & Wobbe, F. (2013). Generic Mapping Tools: Improved version released. *Eos, Transactions American Geophysical Union*, *94*(45), 409–410. https://doi.org/10.1002/2013EO450001

Wicks, C. W., Thatcher, W., Dzurisin, D., & Svarc, J. (2006). Uplift, thermal unrest and magma intrusion at Yellowstone caldera. *Nature*, *440*(7080), 72–75. https://doi.org/10.1038/nature04507

Zhan, Y., & Gregg, P. M. (2017). Data assimilation strategies for volcano geodesy. *Journal of Volcanology and Geothermal Research*, *344*, 13–25. https://doi.org/10.1016/j.jvolgeores.2017.02.015

Zhan, Y., & Gregg, P. M. (2019). How accurately can we model magma reservoir failure with uncertainties in host rock rheology? *Journal of Geophysical Research: Solid Earth*, *124*(8), 8030–8042. https://doi.org/10.1029/2019JB018178

Zhan, Y., Gregg, P. M., Le Mével, H., Miller, C. A., & Cardona, C. (2019). Integrating Reservoir Dynamics, Crustal Stress, and Geophysical Observations of the Laguna del Maule Magmatic System by FEM Models and Data Assimilation. *Journal of Geophysical Research: Solid Earth*, *124*(12), 13547–13562. https://doi.org/10.1029/2019JB018681

Zhan, Y., Gregg, P. M., & Lu, Z. (2021). Modeling magma system evolution during 2006–2007 volcanic unrest of Atka Volcanic Center, Alaska. *Journal of Geophysical Research: Solid Earth*, *126*(2), 1–19. https://doi.org/10.1029/2020JB020158

Zhang, Z. (2002). An empirical relation between mode I fracture toughness and the tensile strength of rock. *International Journal of Rock Mechanics and Mining Sciences*, *39*(3), 401–406. https://doi.org/10.1016/S1365-1609(02)00032-1